The Structure of
Random Ellipsoid Packings

Diploma thesis

Fabian Schaller

4. Mai 2012

Institut für Theoretische Physik
Friedrich-Alexander Universität
Erlangen-Nürnberg

Supervisors:
Dr. Gerd Schröder-Turk
Dr. Matthias Schröter
Prof. Dr. Klaus Mecke

Abstract

Disordered packings of ellipsoidal particles are an important model for disordered granular matter and can shed light on geometric features and structural transitions in granular matter. In this thesis, the structure of experimental ellipsoid packings is analyzed in terms of contact numbers and measures from mathematical morphometry to characterize of Voronoi cell shapes. Jammed ellipsoid packings are prepared by vertical shaking of loose configurations in a cylindrical container. For approximately 50 realizations with packing fractions between 0.54 and 0.70 and aspect ratios from 0.40 to 0.97, tomographic images are recorded, from which positions and orientations of the ellipsoids are reconstructed. Contact numbers as well as discrete approximations of generalized Voronoi diagrams are extracted. The shape of the Voronoi cells is quantified by isotropy indexes $\beta_\nu^{r,s}$ based on Minkowski tensors. In terms of the Voronoi cells, the behavior for jammed ellipsoids differs from that of spheres; the Voronoi Cells of spheres become isotropic with increasing packing fraction, whereas the shape of the Voronoi Cells of ellipsoids with high aspect ratio remains approximately constant. Contact numbers are discussed in the context of the jamming paradigm and it is found that the frictional ellipsoid packings are hyperstatic, i.e. have more contacts than are required for mechanical stability. It is observed, that the contact numbers of jammed ellipsoid packings predominantly depend on the packing fraction, but also a weaker dependence on the aspect ratio and the friction coefficient is found. The achieved packing fractions in the experiments lie within upper and lower limits expected from DEM simulations of jammed ellipsoid packings. Finally, the results are compared to Monte Carlo and Molecular Dynamics data of unjammed equilibrium ellipsoid ensembles. The Voronoi cell shapes of equilibrium ensembles of ellipsoidal particles with a low aspect ratio become more anisotropic by increasing the packing fraction, while the cell shape of particles with large aspect ratios does the opposite. The experimental jammed packings are always more anisotropic than the corresponding densest equilibrium configuration.

Zusammenfassung

Amorphe Packungen ellipsoidförmiger Teilchen sind ein wichtiges Modell für ungeordnete Granulate. Ihr Studium ergibt Aufschluss über geometrische Eigenschaften und Strukturübergänge in granularen Medien. In dieser Diplomarbeit wird die Struktur der Packungen aus Ellipsoiden bezüglich typischer Kontaktzahlen und Form-Maßen aus der mathematische Morphometrie zur Charakterisierung der Voronoi-Zellen analysiert. Amorphe mechanisch stabile Packungen von Ellipsoiden werden durch vertikales Schütteln loser Packungen in einem zylinderförmigen Behälter erzeugt. Circa 50 Packungen mit Packungsdichten zwischen 0.54 und 0.70 und Achsenverhältnissen zwischen 0.40 und 0.97 werden per Tomographie untersucht. Aus den 3D Tomogramm-Realraumdaten werden die Positionen und Orientierungen rekonstruiert. Kontaktzahlen sowie diskrete Approximationen von verallgemeinerten Mengen-Voronoi Diagrammen werden extrahiert. Die Form der Voronoi-Zellen wird mit Anisotropie-Maßen $\beta_\nu^{r,s}$, welche auf Minkowski Tensoren basieren, analysiert. Das Verhalten für amorphe Packungen von Ellipsoiden unterscheidet sich von dem von Kugeln bezüglich der Voronoi-Zellen. Die Voronoi-Zellen von Kugeln werden mit Erhöhung der Packungsdichte isotroper, wohingegen die Form der Voronoi-Zellen von Ellipsoiden mit hohem Achsenverhältnis ungefähr konstant bleibt. Die Kontaktzahlen werden im Sinne des "Jamming Paradigms" diskutiert. Es wird gezeigt, dass Packungen mit reibungsbehafteten Ellipsoiden hyperstatisch sind, das heißt sie haben mehr Kontakte, als sie für die mechanische Stabilität benötigen. Wir sehen, dass die Kontaktzahlen von "gejammten" Ellipsoid-Packungen in erster Linie von der Packungsdichte abhängt. Es wird aber auch eine schwächere Abhängigkeit von dem Aspektverhältnis und dem Reibungskoeffizienten beobachtet. Die erzielten Packungsdichten liegen zwischen den Werten für die höchste und niedrigste Packungsdichte, welche in DEM-Simulationen vorhergesagt wurden. Zum Schluss werden die Ergebnisse mit Daten aus Monte Carlo und Molekular Dynamik Simulationen für Gleichgewichtsensemble verglichen. Die Form der Voronoi-Zellen von Gleichgewichtsensemblen von Ellipsoiden mit kleinem Achsenverhältnis wird bei Erhöhung der Packungsdichte anisotroper, wohingegen die Form der Voronoi-Zellen für Ellipsoide mit großen Achsenverhältnissen sich gegenteilig verhält. Die experimentellen amorphen Packungen sind immer anisotroper als die entsprechende Gleichgewichtskonfiguration.

Contents

Introduction

How many candies are in the bag? How many objects of a given shape can you pack into a container? These questions are interesting for children as well as for scientists. Children aim for as many candies as possible in their bag. Scientists are, for example, interested in finding efficient ways to pack objects or in understanding what prevents the formation of the most efficient packing.

For granular media the understanding of packing phenomena of simple objects is important, as it provides models for the understanding of packing effects of more complex shapes, such as those found in sand or stones. The rigidity of granular matter is relevant for geological processes, including avalanches and landslides [34].

The simplest convex object is a sphere. Therefore a large number of studies on packing phenomena have focused on sphere packings. Packing phenomena of spherical particles, such as the existence of a fairly sharp maximal packing fraction for disordered packings (*random close packing* [9, 78]) or the *jamming transition* from freely flowing to rigid sphere configurations [58, 86], have been studied numerically and experimentally. They are quiet well understood but with some detail still under debate. However, spheres are only the simplest model with obvious differences to the possible anisotropic shapes found in sand or stones. Spheres are also special in terms of their rotational symmetry in all directions, that effects the degrees of freedom.

The study of aspherical particle ensembles offers the possibility to assess the effect of the particle shape on the packing properties. Obvious generalizations of spheres are ellipsoids, packings of which are the subject of this thesis. Other particles shapes are tetrahedra [26, 55] or superellipsoids [14].

The properties of random packings of frictionless ellipsoids have been studied with different types of simulation [14, 16, 17]. Recently, a Discrete Element Simulation for the simulation of frictional ellipsoid packings was described [15]. Packing experiments on ellipsoid packings were only performed with two different types of ellipsoidal particle shapes, with the packing fraction being the only quantity that has been thoroughly investigated [16, 18].

With few exceptions, all current knownledge about packings of ellipsoidal particles stems from numerical simulations, with quantitative experiments few and far between. This thesis reports on packing properties of experimental ellipsoidal particles imaged by X-ray tomography. Packing experiments are performed with ellipsoidal particles of different materials and aspect ratios. Tomographic images of the packings are recorded, reconstructed and the particles are detected. A deeper understanding of the geometric structure is obtained by the analysis with different geometrical measures, including contact numbers or anisotropy measures based on Minkowski tensors.

Chapter 1 provides an introduction about packing phenomena of spheres and ellip-

soids. Furthermore the anisotropy analysis with Minkowski Tensors is described. The preparation methods, the tomographic imaging and the particles detection algorithm are explained in chapter 2. Also the methods for calculating the statistical properties such as packing fraction, contact numbers and anisotropy of the packing are explained. Chapter 3 analyzes the statistical properties of the experimental datasets and compares them to published numerical results. Finally, chapter 4 provides a summary that discusses the specific findings with reference to important open questions of the field of granular matter.

1 Properties and Structure of Disordered Packings

Packings of granular material are an important topic in engineering and physics [7]. Granular media as well as foams, colloidal suspensions, glasses, etc. can *jam*, that is, build a rigid disordered state that withstands finite shear stress before yielding. The transition from the flowing to the jammed state is called the *jamming transition* [86].

The average contact number between the particles in a system is a conceptually simple topological quantity that is well studied, for example with respect to the stability or rigidity of a system [86]. This work refers to the geometrical contact number, i.e. the number of touching particles, in contrast to the mechanical contact number which is the number of contacts per particle that carry forces [82]. The minimum contact number, below which a system looses rigidity, is called *isostatic* contact number z_{iso}. This value can be calculated by a constraint counting argument: z_{iso} is the minimum number of contacts, for which no floppy deformations can exist in the system. Floppy deformations are deformations which do not cost elastic energy [86].

1.1 Jammed Sphere Packs

The packing properties of spheres are well investigated because of being the simplest convex object. The important experimental, theoretical and numerical results are summarized in this section.

It is numerically shown that *frictionless* hard spheres can only form jammed[1] disordered packings with a packing fraction of $\Phi_J \approx 0.64$ at the so-called point J. The point J is defined as the point of the jamming transition for an infinite system of frictional spheres [58]. Denser and fully disordered systems of spheres can only be achieved for soft spheres by compression. The *jamming paradigm* states that properties like the packing fraction or the contact number scale to point J [86]. Numerically it was found that frictionless spheres reach isostaticity at Point J with an average contact number of $z_{iso} = 6$ (see refs. [58, 86] for details).

Amorphous packings of *frictional* hard spheres can be prepared in a finite interval of packing fractions. This was first established by Bernal and Scott [9, 78]. The lower bound is referred to as the *Random Loose Packing* (RLP) limit with a packing fraction of $\Phi_{RLP} \approx 0.55$. Below this limit, no mechanically stable random packing exists [35]. The densest amorphous packing which can be obtained with experimental methods

---

[1] For spheres, several different notions of jamming can be distinguished like local, collective or strict jamming. For further information see ref. [85].

has a packing fraction of $\Phi_{\text{RCP}} \approx 0.64$ [78]. This upper bound is named *Random Close Packing* (RCP) and coincides with point J. For frictional particles, the isostatic contact number (the minimal number of contacts to give rigid structures) is $z_{\text{iso}} = 4$. Random packings of frictional hard spheres are generally *hyperstatic*, i.e. have an average contact number larger than z_{iso} [86]. The average contact number of sphere packings has been analyzed previously for simulated data [36, 58, 86] as well as in experiments on amorphous sphere packs [5, 6].

Packings above the Random Close Packing limit contain crystalline domains. For spheres, the densest possible crystalline packings are known. These are the fcc or hcp packings resulting in a packing fraction of $\Phi_{\text{fcc}} \approx 0.74$ [27]. It is by now largely established that static jammed sphere packings show a "phase transition" at $\Phi_{\text{RCP}} = \pi/\sqrt{18} \approx 0.64$, the critical packing fraction at which formations of crystalline fcc or hcp clusters first occurs [36, 37]. This phase transition, in an athermal ensemble first proposed by Edwards and co-workers [19], is analogous to the first order phase transition in thermal hard spheres, with a critical packing fraction where crystallization occurs [64]. The measurement of the order and crystallinity of a sphere packing is a well investigated field. Different methods have been devised, i.e. the widely used bond-orientational order parameter Q_l defined by Steinhard *et. al* [84] or methods based on Minkowski tensors [37, 38, 77]. These order metrics are all defined with reference to the known densest crystal phases of spheres.

In this thesis, the degree of order of a packing is measured by characterizing the Voronoi cells of the particles with the anisotropy indexes $\beta_\nu^{r,s}$ based on the Minkowski tensors, see section 1.4. In previous work, it was found that the Voronoi cells of sphere packs are anisotropic [77]. The anisotropy indexes $\beta_\nu^{r,s}$ can also be used to characterize systems of equilibrium hard sphere fluids [38].

1.2 Jammed Ellipsoid Packs

An obvious generalization of spheres are ellipsoids. This chapter provides an overview of previous work on jamming of ellipsoidal particles.

Ellipsoids can be classified into three different categories namely oblate, prolate and fully aspherical ellipsoids. An oblate ellipsoids is a rotationally symmetric ellipsoid with two identical shorter half-axes and one longer one. Prolate ellipsoids have two short axes and one longer axis. For oblate and prolate ellipsoids, the aspect ratio α is defined as the ratio of the length of the individual axis to the length of the identical ones. Fully aspherical ellipsoids are ellipsoids with three different axis lengths.

Investigations of the packing properties of hard ellipsoids have been done by Donev et. al [16]. In their study, the Lubachevsky-Stillinger sphere-packing algorithm[2] was generalized from frictionless spheres to frictionless ellipsoids. The result of this algorithm are densest random packings for each aspect ratio, see figure 1.1-A. The plot shows the packing fraction for jammed frictionless ellipsoids. It can be seen that

---

[2] Hard-particle molecular dynamics algorithm. Points are randomly distributed and expand uniformly during the simulation until the pressure diverges. The result are dense disordered packings. For further information see refs. [42, 43].
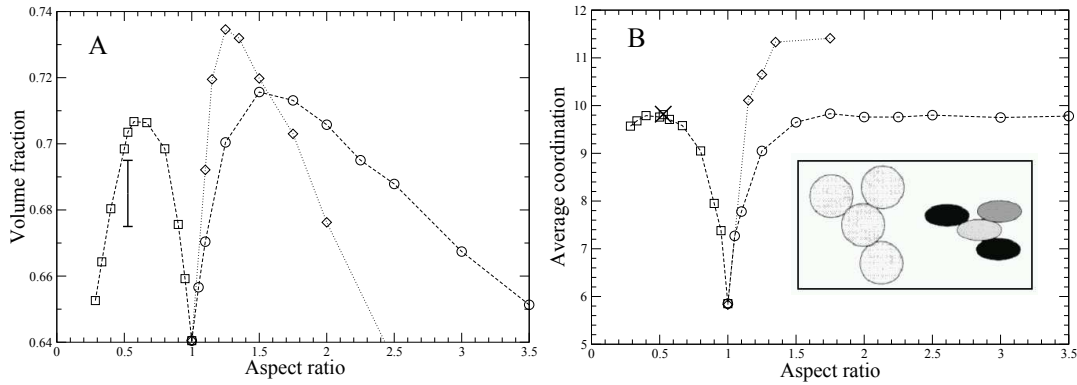
Figure 1.1: **(A)** Packing fraction and **(B)** average contact numbers as a function of the aspect ratio α for jammed ellipsoids configurations created with a generalized Lubachevsky-Stillinger algorithm for oblate ellipsoids (spares), prolate ellipsoids (circles) and fully aspherical ellipsoids (diamonds). Both figures are reproduced from Fig 2 of ref. [16].

the achieved packing fraction depends on the aspect ratio α , e.g. densest random packs of oblate ellipsoids are formed with an aspect ratio of about 0.65, see figure 1.1-A.

A suggested explanation for the fact, that ellipsoids can pack more densely than spheres was derived from the fact, that the Voronoi cells of sphere packs are anisotropic [77]. That reference suggested, that the anisotropic average cell shape of sphere packs could provide an explanation for the observed higher packing fraction in *disordered* ellipsoid packs: Given an inherently anisotropic shape of each Voronoi cell (even when the particles are spheres, i.e. isotropic) it appears intuitive to assume that anisotropic particles (such as ellipsoids) give a better fit with the anisotropic Voronoi cell (if suitable aligned), and hence a higher packing fraction.

The average contact number of the particles is shown in figure 1.1-B. The isostatic contact number for packings of frictionless prolate and oblate ellipsoids is $z_{\mathrm{iso}} = 10$ (for fully aspherical: $z_{\mathrm{iso}} = 12$) [16]. It can be observed that packings of frictionless, slightly ellipsoidal particles are highly *hypostatic*, i.e. have less contacts than the isostaticity condition requires. Hypostatic packings should not be able to form a jammed packing because they are mechanically underconstrained without resistance if a force is applied forces in the direction of floppy modes. However, it has already been demonstrated that particles with sufficiently flat curvature at the point of contact can jam in hypostatic packings [17]. In the frictional case, the isostatic contact number z_{iso} changes to 4 because there are tangential forces at the contacts [86].

The numerical results of ref. [16] have been reproduced by Discrete Element Method[3] (DEM) simulations [14]. A DEM simulation was also used to simulate frictional ellipsoids settling into a rectangular container filled with a viscous liquid [15].

---

[3] Computation of the forces acting on each particle (collisions, friction, ..) and solving of the equations of motion, possibly under gravity and with particles immerse in a viscous fluid. (references are given in [14, 15])

The simulation has been done for frictionless ellipsoids and for ellipsoids with an extremely high friction coefficient. The viscosity was varied in the simulations. For frictionless ellipsoids, the results were found to be independent of the viscosity. The packing fraction of frictional ellipsoids decreases when increasing the viscosity until a constant value is reached. This new lower limit for the packing fraction was named *sedimented loose packing limit* Φ_{SLP} [15].

For spheres the densest crystalline packing (fcc or hcp) is known, but not for ellipsoids. The analysis of equilibrium ellipsoids can provide some information about crystalline solid phases. The first phase diagram of ellipsoids has been provided by Frenkel & Mulder [21, 22]. It basically consists of four phases: a solid phase assumed to be a streched-fcc, a so-called plastic solid phase with position but no orientationally order of the ellipsoids, a nematic fluid i.e. orientationally but no position ordered ellipsoids and an isotropic fluid. Further investigations revealed new crystal phases and the achievable packing density has increased. A new crystal structure (SM2) with a very high packing fraction was found. It has a simple monoclinic unit cell containing two ellipsoids of unequal orientation [18, 61, 65]. Also crystal phases of ellipsoids on a regular lattice have been studied [66]. Until now, not all (especially the densest) crystalline phases of ellipsoids are known. Thus, a measure of the degree of crystallinity and order for an ellipsoid pack is harder to define than for spheres where fcc and hcp are the only densest crystalline structures.

Donev *et. al* compared their numerical results to experimental data of experiments with two different types of ellipsoidal particles. The packing of two sorts of M&M's Milk Chocolate candies[4] with aspect ratios of 0.51 and 0.53. Additionally, ellipsoids fabricated using a stereolithography machine with aspect ratio 1.25:1:0.8 have been analyzed [16, 45]. For packings of M&M's Milk Chocolate candies, an agreement in the contact number between the experiment and the results of the simulations has been found (see cross in figure 1.1-B). This is unexpected given that the experimental ellipsoids are frictional, in contrast to the simulation which is for frictionless ellipsoids. In the packing fraction a deviation to the numerical data can be observed (see error bar in figure 1.1-A).

1.3 Generalized Voronoi Diagrams

The problem of jamming and packing of hard particles is a very geometric one - with physical interactions reduced to hard core repulsion (at least for frictionless particles without gravity). Because of this geometric nature, it is particularly important to have succinct methods to quantify structure and shape, both globally and locally. Topological contact number and neighborhoods, discussed at length in section 2.6, are one approach to this end. A different approach, which is also used in this thesis, is through the construction of Voronoi diagrams. Here, the construction of Voronoi diagrams for non-spherical particles is discussed.

For an ensemble of spherical objects of the same radius, the Voronoi cells are defined by the Voronoi tessellation of the particle centers. All locations in space are associated

---

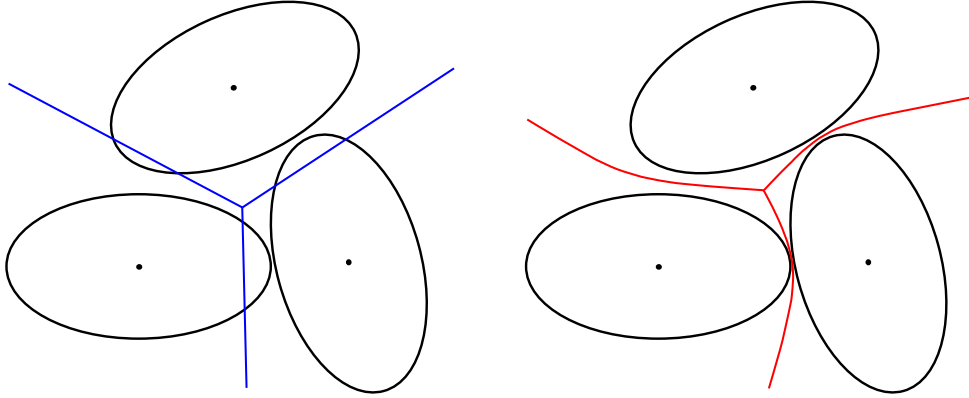[4]registered trademark of Mars Inc.

Figure 1.2: Construction of the Set Voronoi Diagram for ellipsoids: Difference between the normal Voronoi Diagram of the ellipsoids center points (left plot, blue lines) and the Set Voronoi diagram of the ellipsoids (right plot, red lines) of three ellipsoidal particles. While the normal Voronoi diagram facets may intersect with the ellipsoidal particles, the facets of the Set Voronoi Diagram trace loci of equal distance to the ellipsoid surfaces.

to the object of closest distance to the center. The resulting so-called *Voronoi cells* are convex polytopes [59]. For objects which are not spherical or not monodisperse the Voronoi diagram needs to be generalized [59].

For polydisperse spheres the *Laguerre diagram* can be used, where the distance of the facet to the center is weighted with the radius [59].

For non-spherical objects an even more generalized Voronoi diagram is needed [44, 59]. The generalization can be done with the following assignment rule [59]: the void space is assigned to the object with the closest distance to the surface. By this generalization the facets of the Voronoi Cell may be curved and the Cell is no longer a convex polytope. As it can be seen this tessellation is different from the normal Voronoi tessellation, where the space is assigned to the object with closest distance to the center. In 2D, the corresponding Voronoi diagram is called *area Voronoi diagram* [59]. In reference to that, we call this generalized Voronoi diagram in the 3D case *Set Voronoi diagram*. The difference between the normal and the Set Voronoi diagram in illustrated in figure 1.2. The calculation of the Set Voronoi diagram is described in section 2.7.

In this work the Set Voronoi diagram is analyzed with anisotropy measures $\beta_\nu^{r,s}$ based on the Minkowski Tensors.

1.4 Structure analysis by Minkowski tensors[5]

This section describes the structure analysis with Minkowski tensors for arbitrary objects K. For the analysis of ellipsoid configurations the objects K represent the Voronoi cells of the particles.

---

[5]Most of this section is an almost verbatim extract of ref. [76] of which I am co-author.

1.4.1 Minkowski Tensors

The definition of Minkowski functionals is built on the strong mathematical foundation of integral and convex geometry, both for the scalar functionals [25, 70, 71, 72] and for the tensor-valued functionals [2, 29, 30]. The mathematical definition based on so-called *fundamental measure theory* is equivalent to a more intuitive definition based on surface integrals that has been more popular for the application of Minkowski functionals in the physical sciences, pioneered by Mecke [49, 51, 52, 54]. This section provides an overview of the definition of Minkowski tensors and of their essential properties.

Generally, a shape index is a function that takes a spatial object as the argument and produces a value that quantifies some aspect of the shape of the object. Minkowski functionals are shape indices in this sense for the specific situation where the object is a solid body K (in this thesis, the Voronoi cells of the ellipsoids) bounded by a bounding surface ∂K, mathematically speaking a compact set with non-empty interior embedded in Euclidean space $\mathbb{E}^3$. This definition includes in particular bodies with a discretized, e.g. triangulated bounding surface, with curvature and normal discontinuities at the edges. The value of a shape index is not necessarily a single number, e.g. for the radial two-point correlation function $g_2(r)$ it is a real-valued function. For scalar Minkowski functionals, however, the value is just a single real-valued number and for tensorial Minkowski functionals it is a tensor, here specifically a symmetric rank-two tensor with six independent real-valued components. Other examples of tensorial shape indices of rank two defined for a body K are the tensor of inertia $\mathbf{I}$ [23], the mean intercept length tensor $\mathbf{MIL}(K)$ [12, 28, 32, 48, 57, 87, 88], see also Ref. [40], and the quadrupole tensor $\mathbf{Q}$ [33], see also Ref. [56].

Tensorial Minkowski functionals are the generalization of the scalar Minkowski functionals to tensorial quantities. Obvious applications are physical systems with explicit orientation dependence including anisotropy and orientational ordering, effective mechanical properties of inhomogeneous materials, etc. While in principle defined for arbitrary rank, the current focus are Minkowski tensors of rank two. An intuitive generalization of the scalar functionals $W_0 \propto \int_K dV$ and $W_\nu(K) \propto \int_{\partial K} g_\nu dA$ (for $\nu = 1, \ldots, 3$) is achieved by introducing tensor products of position vectors $\mathbf{r}$ and surface normal vectors $\mathbf{n}$ into the integrals ($g_1 = 1$. g_2 and g_3 are the point-wise mean and Gaussian curvature of the bounding surface ∂K, possibly their discrete equivalents applicable to polyhedra). For spatial geometries there are six relevant linearly-independent tensors

$$\mathbf{W}_0^{2,0}(K) := \int_K \mathbf{r} \otimes \mathbf{r}\, \mathbf{dV}, \tag{1.1}$$

$$\mathbf{W}_1^{2,0}(K) := \frac{1}{3} \int_{\partial K} \mathbf{r} \otimes \mathbf{r}\, \mathbf{dA}, \tag{1.2}$$

$$\mathbf{W}_2^{2,0}(K) := \frac{1}{3} \int_{\partial K} H(\mathbf{r})\, \mathbf{r} \otimes \mathbf{r}\, \mathbf{dA}, \tag{1.3}$$

$$\mathbf{W}_3^{2,0}(K) := \frac{1}{3} \int_{\partial K} G(\mathbf{r})\, \mathbf{r} \otimes \mathbf{r}\, \mathbf{dA}, \tag{1.4}$$

$$\mathbf{W}_1^{0,2}(K) := \frac{1}{3} \int_{\partial K} \mathbf{n} \otimes \mathbf{n} \; d\mathbf{A}, \tag{1.5}$$

$$\mathbf{W}_2^{0,2}(K) := \frac{1}{3} \int_{\partial K} H(\mathbf{r}) \, \mathbf{n} \otimes \mathbf{n} \; d\mathbf{A}. \tag{1.6}$$

Here, $H(\mathbf{r}) = (\kappa_1 + \kappa_2)/2$ and $G(\mathbf{r}) = (\kappa_1 \kappa_2)$ are the mean and Gaussian curvature of ∂K and $\otimes$ the tensor product defined as $(\mathbf{a} \otimes \mathbf{a})_{ij} = a_i a_j$ for any vector $\mathbf{a}$ (note that this is equivalent for these tensors to the conventional definition with a symmetric tensor product [74]). Note that the labels ν, r, s define different tensors and are not the indices of its components; the components are indexed by i, j and denoted $(\mathbf{W}_\nu^{r,s})_{ij}$. The label ν represents the same integral types as for the scalar Minkowski functionals ($\nu = 0$ the volume integral, $\nu = 1$ the surface integral, $\nu = 2$ the mean-curvature weighted surface integral, etc) and r and s the tensorial powers of the position and surface normal vectors, respectively. Generalizing Hadwiger's statement, Alesker's theorem states, that all motion-covariant, conditionally continuous, and additive tensorial functionals $\mathbf{F}(K)$ can be expressed as a linear combination of the Minkowski tensors listed above and the scalar functionals multiplied by the rank-two unit tensor [2]. This list of tensors has also been shown to be linearly independent [30].

The definition of the Minkowski tensors provides a set of four (six) truly tensorial shape indices for planar (spatial) bodies. The different aspects of the morphology that these tensors capture can be intuitively understood, see Figure 1.3. The tensors $\mathbf{W}_\nu^{2,0}$ bear a resemblance to the tensor of inertia $\mathbf{I}(K) = \int_K (-\mathbf{r} \otimes \mathbf{r} + |\mathbf{r}|^2 \mathbf{E_3}) \; d\mathbf{V} = -\mathbf{W}_0^{2,0} + tr(\mathbf{W}_0^{2,0}) \mathbf{E_3}$ with the three-dimensional unit matrix $\mathbf{E_3}$ and tr denoting the trace of a matrix. The tensor $\mathbf{W}_0^{2,0}$ can be interpreted as a so-called *moment tensor* of a solid body K that quantifies the distribution of mass within the body. Similarly, $\mathbf{W}_1^{2,0}$ is the moment tensor of a hollow body with a homogeneous mass distribution on the surface. Further, for spatial polytopes (bounded by closed polygons of straight segments), the tensors $\mathbf{W}_2^{2,0}$ and $\mathbf{W}_3^{2,0}$ are the moment tensors of a wire-frame body and a body with mass located at the vertices, with the mass distributed according to discrete mean curvature (dihedral angles across an edge) and discrete Gaussian curvature (angle deficit around a vertex). As does the tensor of inertia, the Minkowski tensors $\mathbf{W}_\nu^{2,0}$ with $\nu = 0, \ldots, d$ depend on the chosen origin $\mathbf{0}$.

The tensors $\mathbf{W}_1^{0,2}$ and $\mathbf{W}_2^{0,2}$ are translation-invariant; hence the choice of origin is irrelevant for these tensors. In contrast to the tensors $\mathbf{W}_\nu^{2,0}$, their morphological interpretation is not the distribution of mass but the orientational distribution of surface patches and curvatures. This is evident for the simple planar example where the body K is a rectangular prism of size $L_x \times L_y \times L_z$ aligned with the coordinate axes; the tensor $\mathbf{W}_1^{0,2}$ is diagonal with components $(\mathbf{W}_1^{0,2})_{xx} \propto L_y$, $(\mathbf{W}_1^{0,2})_{yy} \propto L_x$ and $(\mathbf{W}_1^{0,2})_{zz} \propto L_z$, reflecting the portions of interface oriented along the three orthogonal directions. For more general bodies K, the following considerations illustrate the relationship between $\mathbf{W}_1^{0,2}$ and the orientation distribution, see also Figure 1.3e. Given a body K with boundary ∂K we define the function

$$\omega(K,\mathbf{n}') = \frac{1}{2} \int_{\partial K} \delta(\mathbf{n}(\mathbf{r}) - \mathbf{n}') \; d\mathbf{r} \tag{1.7}$$
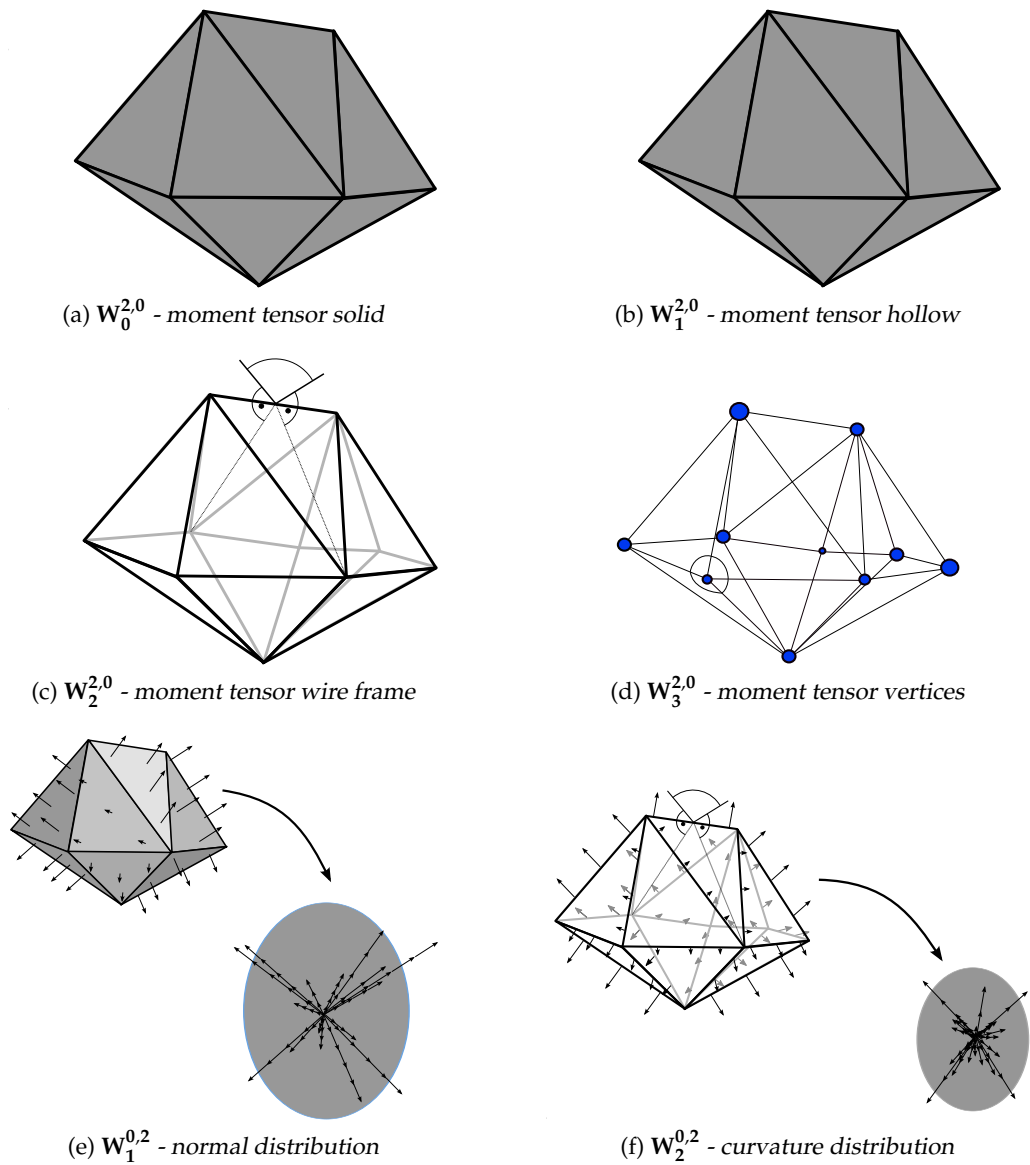
(a) $\mathbf{W}_0^{2,0}$ - *moment tensor solid*

(b) $\mathbf{W}_1^{2,0}$ - *moment tensor hollow*

(c) $\mathbf{W}_2^{2,0}$ - *moment tensor wire frame*

(d) $\mathbf{W}_3^{2,0}$ - *moment tensor vertices*

(e) $\mathbf{W}_1^{0,2}$ - *normal distribution*

(f) $\mathbf{W}_2^{0,2}$ - *curvature distribution*

Figure 1.3: Geometric meaning of the six linearly independent Minkowski tensors for 3D polyhedral bodies. While the tensors $\mathbf{W}_\nu^{2,0}$ characterize mass distributions of solid ($\mathbf{W}_0^{2,0}$), hollow ($\mathbf{W}_1^{2,0}$), wireframe ($\mathbf{W}_2^{2,0}$) or point-vertex cells ($\mathbf{W}_3^{2,0}$), the tensors $\mathbf{W}_1^{0,2}$ and $\mathbf{W}_2^{0,2}$ characterize surface normal distributions.

where $\delta(\mathbf{x})$ is Dirac's delta distribution and $\mathbf{n}(\mathbf{r})$ the normal vector of ∂K at $\mathbf{r}$. The function $\omega(K,\mathbf{n}')$ is the density function of normal directions of the bounding curve ∂K, i. e. $\omega(K,\mathbf{n}')$ is the total length of all those patches of ∂K that have normal direction $\mathbf{n}'$. It is normalized to the total surface area $W_1(K)$, i.e. $\int_{\mathbb{S}^1} \omega(K,\mathbf{n}) \, \mathbf{dn} = W_1(K)$.

We can now rewrite the Minkowski tensor $\mathbf{W_1^{0,2}}$ as

$$\mathbf{W_1^{0,2}}(K) = \frac{1}{2} \int_{\partial K} \mathbf{n} \otimes \mathbf{n} \, \mathbf{dr} \tag{1.8}$$

$$= \frac{1}{2} \int_{\partial K} \mathbf{n} \otimes \mathbf{n} \int_{\mathbb{S}_2} \delta(\mathbf{n} - \mathbf{n}') \, \mathbf{dn}' \, \mathbf{dr}$$

$$= \int_{\mathbb{S}_2} \mathbf{n} \otimes \mathbf{n} \, \omega(K,\mathbf{n}) \, \mathbf{dn} \tag{1.9}$$

with the unit sphere $\mathbb{S}_2$. This shows that the Minkowski tensor $\mathbf{W_1^{0,2}}$ is an integral tensorial characterization of the normal vector distribution. Further detail is described in Refs. [73, 74].

1.4.2 Algorithms for Minkowski Tensors

Fast linear-time algorithms for the computation of Minkowski tensors applicable to polygonal representations of a given body K are available [11, 73, 74], analogous to algorithms for their scalar counter-parts [4, 24, 39, 46, 50, 53]. These algorithms yield expressions for the Minkowski tensors of the body bounded by the triangulated surface, that are accurate up to the numerical precision. For bodies bounded by polygonal flat facets, typically triangles, that necessarily have curvature discontinuities along the facets' edges and vertices these algorithms are derived for convex bodies by considering parallel surfaces and parallel bodies with continuous curvature properties in the limit of vanishing thickness. Derived for convex bodies, their validity for non-convex bodies is a consequence of the additivity of the Minkowski tensors.

The Minkowski Tensors of the Voronoi cells are calculated with *Karambola*. Karambola is a computer software able to calculate Minkowski Tensors of three-dimensional bodies and surfaces. It is developed at the Institute of Theoretical Physics in Erlangen, largely implemented by Sebastian Kapfer and me. It is available as free software (`http://theorie1.physik.uni-erlangen.de/karambola`). In this work version 1.5 is used.

1.4.3 Anisotropy and Shape Indices

While the natural format of an orientation-dependent physical property is tensorial, it can be more convenient to reduce the tensorial shape indices to scalar indices. In particular, the Minkowski tensors can be used as succinct and comprehensive anisotropy indices of a spatial structure. In this case, the degree of anisotropy of a given body K is conveniently expressed as the ratio of minimal to maximal eigenvalue of the Minkowski tensors

$$\beta_\nu^{r,s} := \frac{|\mu_{\min}|}{|\mu_{\max}|} \in [0,1], \tag{1.10}$$

where $\mu_{\min}$ and $\mu_{\max}$ are the eigenvalues of $\mathbf{W}_\nu^{\mathbf{r,s}}$ with minimal and maximal absolute value. Note that for non-convex planar bodies the tensor $\mathbf{W}_2^{2,0}$ may have negative eigenvalues.

With this notation, a body that is isotropic with respect to the tensor $\mathbf{W}_\nu^{\mathbf{r,s}}$ corresponds to $\beta_\nu^{r,s} = 1$ and deviations from unity indicate the degree of anisotropy.

Importantly, there is a distinct difference between this notion of *anisotropy* and the notion of *asphericity* [83]. Asphericity quantifies the deviations of a shape from a sphere (of the same volume). Cubes, equilateral tetrahedra, etc. are aspherical. The concept of asphericity has a certain ambiguity, in that one can define an ellipsoid with axes $(a,a,b \neq a)$ that gives the same asphericity as a cube, w.r.t. specific measures of asphericity. Anisotropy quantifies the degree of orientational differences in a tensorial sense, i.e. if the body appears identical w.r.t. a particular property from any two planar or three spatial orthogonal directions, it is isotropic. Cubes, tetrahedra, spheres, etc. are isotropic w.r.t. this definition.

The concept of Minkowski tensors leads to the definition of a whole set of anisotropy indices, rather than a unique definition of a single index. This is well-justified by the observation that the degree of anisotropy of a given object may differ depending on which quality of the body is analyzed, e.g. surface orientation or mass distribution; see also the discussion on page 9. The availability of a set of shape indices, that are comprehensive in the sense defined above, allows for a rigorous anisotropy analysis not restricted to one specific morphological quality. Importantly, if an anisotropy analysis by Minkowski tensors yields the same dependence of *all* tensors $\mathbf{W}_\nu^{\mathbf{r,s}}$, this supports the statement that the anisotropy of the system is generic and not subject to the specific method used to quantify it.

2 Tomography and Structure Analysis of Ellipsoid Packings

This chapter describes the experimental preparation of jammed ellipsoid packings, the types of ellipsoid materials used, the image analysis, the detection algorithm and the methods to calculate structural properties.

Loose jammed packings of ellipsoidal particles with different aspect ratios and friction coefficients produced by 3 different methods are prepared in a cylindrical container. By periodic vertical tapping of the container, the packing can be further compactified. With this method packings of different packing fraction can be created by varying the number of taps. The configurations are imaged by X-Ray tomography. Based on the resulting 3D grayscale image the particle center points, sizes and orientations are reconstructed. Statistical properties such as the packing fraction, the contact numbers and the anisotropy of the local environments are calculated. This chapter discusses the methods for computing these quantities.

2.1 Particle Types and Materials

For the experiments ellipsoidal particles of different materials (different friction coefficient) comprising several aspect ratios are used, see also figure 2.1 and tabular 2.1.

- **Pharmaceutical placebo pills (PPP):**
  Ellipsoidal placebo pills coated with a sugar layer, with surface properties similar to those of smarties or M&M chocolate candies. The variations in size of these particles are very small. These particles are oblate, with axis ratios 0.59 and 0.64 for the two sets.

- **3D printer particles (3DP):**
  Gypsum ellipsoids produced with a 3D printer (Z corporation: Zprinter 650) cured with resin. These particles have a significant rougher surface than the placebo pills, resulting in a higher friction coefficient. They are oblate, with aspect ratios from 0.40 to 0.97.

- **Injection molded ellipsoids (IM):**
  Very small and monodisperse ellipsoids produced by plastic injection molding, with a smooth surface and low friction. These particles have an imperfection where the plastic was injected into the mold. They have axes ratios 1.25:1:0.8 and 1.07:1:0.95 corresponding to the max densest ellipsoids of refs. [16, 17] and the typical anisotropy of sphere pack Voronoi Cells from ref. [77].

A selection of these ellipsoids can be seen in figure 2.1.

(a) *3DP: α = 0.33*

(b) *3DP: α = 0.4*

(c) *PPP: α = 0.59*

(d) *PPP: α = 0.64*

(e) *3DP: α = 0.74*
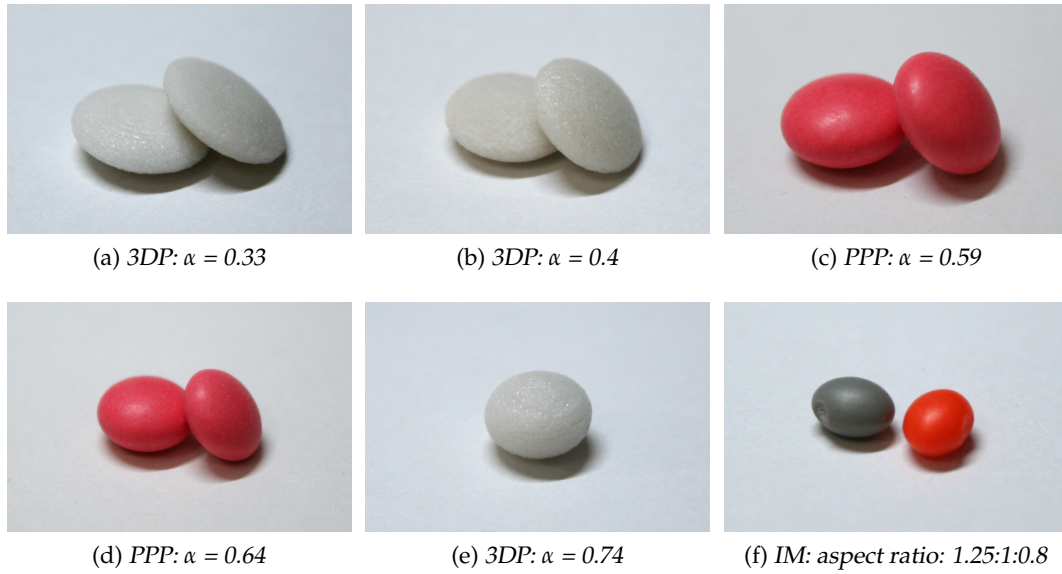
(f) *IM: aspect ratio: 1.25:1:0.8*

Figure 2.1: Some of the different types of ellipsoids and aspect ratios used in the experiments. For oblate ellipsoids i.e. ellipsoids with two long half-axis of the same length, the aspect ratio α is the short axis divided by the long axis. The height of the pictures is about 11mm. (a,b,c) are made by the 3D printer (3DP), (c+d) are pharmaceutical placebo pills (PPP) and (f) is made by injection molding (IM).

aspect	size [mm] ($\pm$ 0.05 mm)			volume		quality	
ratio	e_1	e_1	e_1	[mm^3]	type	q	roughness
0.97	3.2	3.1	3.1	124.8	3DP	0.027	$\geq 32\mu$m
0.91	3.0	3.3	3.3	136.8	3DP	0.024	$\geq 32\mu$m
0.74	2.5	3.5	3.5	128.3	3DP	0.024	$\geq 32\mu$m
0.64	2.0	3.0	3.0	75.4	PPP	0.026	$\approx 2\mu$m
0.60	2.2	3.75	3.75	129.6	3DP	0.024	$\geq 32\mu$m
0.59	2.15	3.55	3.55	113.5	PPP	0.009	$\approx 2\mu$m
0.40	1.6	4.0	4.0	107.2	3DP	0.026	$\geq 32\mu$m

Table 2.1: Properties of the different ellipsoidal particles used in the experiments. For oblate ellipsoids with two half-axes of the same length, the aspect ratio α is defined as the fraction of the short and long axes. It is extracted from the tomographic images. e_1, e_2 and e_3 are the half axes length of the ellipsoids, measured with a sliding caliper. 3DP = 3D printer; PPP = pharmaceutical placebo pill.
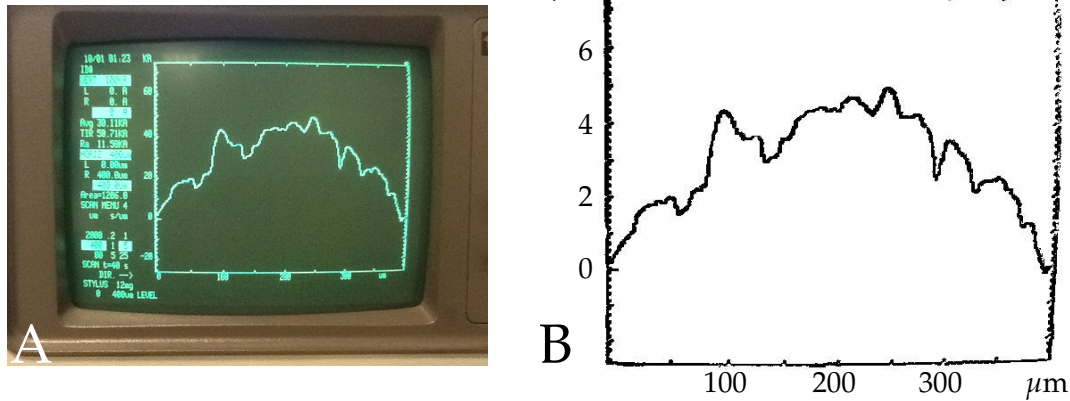
Figure 2.2: Output of a Tencor Instruments Alphastep 250 Profilometer for a surface scan of an pharmaceutical placebo pill. For the 3D printed particles, the depth of the roughness exceeds the vertical range of the profilometer by scanning only a few μm horizontally. (**A**) Display output of the profilometer; (**B**) Extracted data from a photography of the display. (Image recorded using the profilometer of the chair for experimental physics, Prof. Paul Müller, University of Erlangen)

To the naked eye, the surface of the 3D printer particles is rougher than that of the placebo pills. To quantify this surface roughness, the surface of the ellipsoids is scanned with a profilometer (Tencor Instruments Alphastep 250 Profilometer). The output of a surface scan of a placebo pill (aspect ratio $\alpha = 0.59$) is shown in figure 2.2. The surface of the placebo pills is indeed very smooth; the depth of the roughness is about 2 μm. For the 3D printed particles, the depth of the roughness exceeds the vertical range of the profilometer by scanning only a few μm horizontally, where the curvature of the particles has no effect. Hence, the roughness of the 3D printed particles is larger than 32 μm, and these particles are indeed very rough with a high degree of friction.

To check the accuracy of the shape of the particles, the difference between the particle shape imaged by tomography and a perfect ellipsoid is calculated. In figure 2.3 the difference is illustrated in a 3D image for different particles and aspect ratios. White voxels indicate a difference between a perfect ellipsoid and the particle. Figure 2.3b shows that the pharmaceutical placebo pills (PPP) have an almost perfect ellipsoidal shape. The lasting aberrations are due to the discretization of the tomographic image. The 3D printer particles (3DP) show small protrusions at one side of the ellipsoid, see arrows in figure 2.3a and 2.3c.

A good measure for the similarity q of the shape to an ideal ellipsoid is the volume difference V_{diff} between a perfect ellipsoid and the real ellipsoid normalized by the volume V of the perfect ellipsoid:

$$q = \frac{V_{\mathrm{diff}}}{V} \tag{2.1}$$

(a) *3DP: aspect ratio = 0.40*   (b) *PPP: aspect ratio = 0.59*   (c) *3DP: aspect ratio = 0.97*
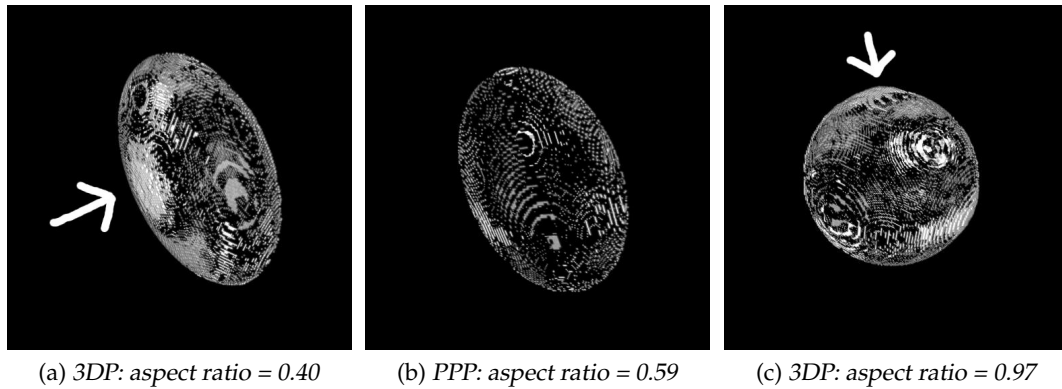
Figure 2.3: Difference between the particle shape, imaged by tomography and a perfect ellipsoid. White voxels indicates the aberration. The placebo pill (b) has a very good ellipsoidal shape. The 3D printer particles (a+c) have a protrusion at one side of the ellipsoid, marked with arrows.

The smaller q, the better the quality of the ellipsoid shape of the particle. The quality values of the different particles are shown in table 2.1.

The injection molded particles have an imperfection into the surface where the plastic was injected into the mold, see Figure 2.4. This imperfection is at the place where the plastic was introduced into the mold. The depth is about 200μm. The imperfection effects the particle detection in the tomographic image and the calculation of discontinuous statistical parameters like the contact number. (Because these particles are not oblate ellipsoids, but rather have three different half-axes, the diagrams in chapter 3 do not contain data based on these particles.)

The measured properties of the different ellipsoidal particles used in the experiments are shown in table 2.1.

Figure 2.4: Imperfection of a plastic injection molded particle.

2.2 Preparation of Jammed Ellipsoid Packings

The ellipsoidal particles are packed into a cylindrical container with a diameter of 104 mm. Different packings are created by different preparation methods and parameters.

Preparation of loose packings

A loose packing is created with the use of a cylindrical cardboard tube which fits tightly into the cylindrical plexiglass container. Figure 2.5 shows pictures of each step. This smaller tube is placed into the container and is slowly filled with ellipsoids poured trough a funnel. Then the tube is pulled out very slowly. Section 3.3 discusses the orientation of the ellipsoids in the resulting packing.
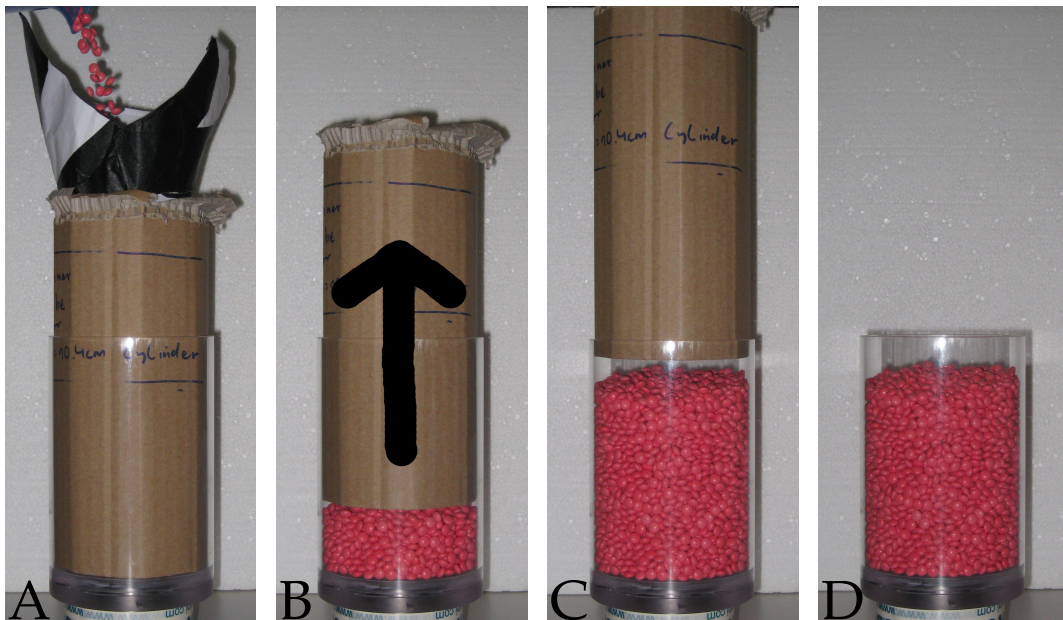
Figure 2.5: Preparation of a loose packing; (**A**) slowly filling the ellipsoids through a cone into a slightly smaller cylindrical cardboard tube; (**B** + **C**) slowly pulling the tube outside; (**D**) resulting loose packing.

Preparation of dense packings by vertical tapping

To create different packings the container can be vertically tapped or shaken. This is done by placing the container on a shaker (LDS - V550 Series Vibrators) connected to a function generator USB-controlled by a computer. The acceleration is controlled by the applied voltage of the function generator. An acceleration sensor which is connected to an oscilloscope measures the acceleration of the container, see figure 2.7.
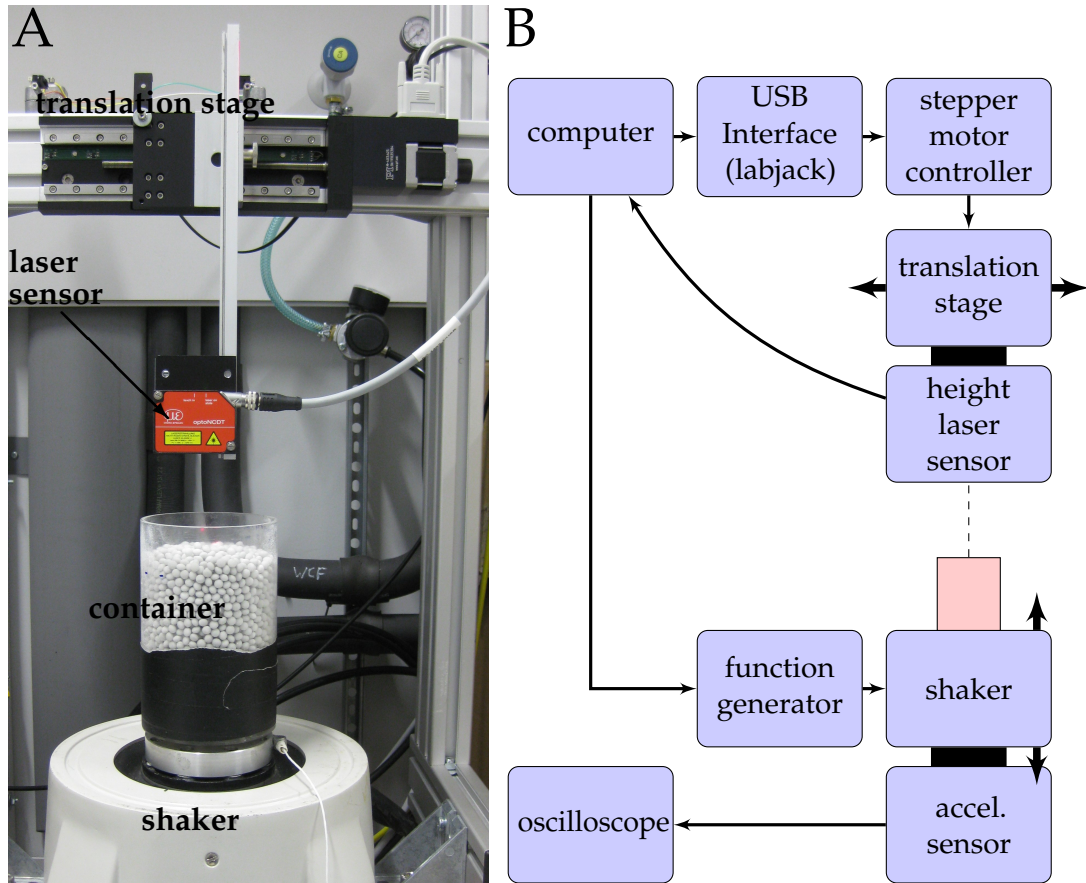
Figure 2.6: Tapping and scanning process of the ellipsoid packings in the cylindrical container; (**A**) shaker setup with translation stage and laser sensor; (**B**) flow diagram of the shaking and scanning setup.
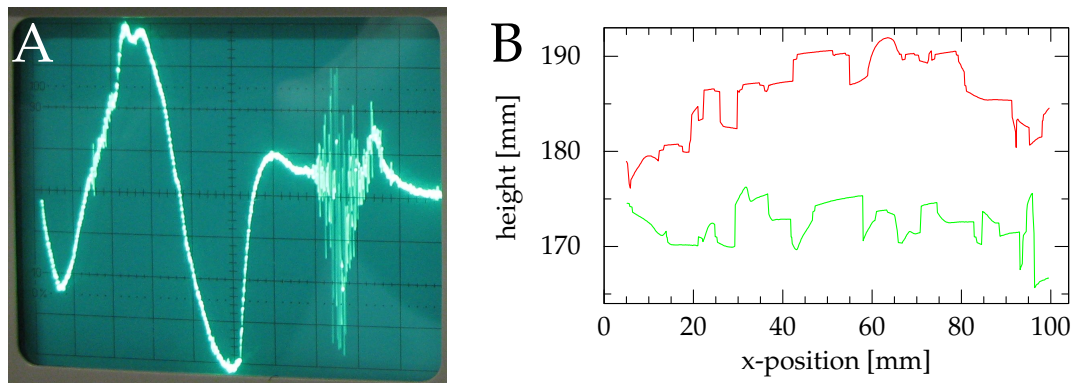
Figure 2.7: (**A**) Output of the oscilloscope monitoring the amplitude and frequency of the shaking (see figure 2.6). One unit in y-direction is 1g and the image shows one cycle. (**B**) One-dimensional profiles as recorded by laser sensor scanning the upper surface of the ellipsoid packing, see figure 2.6. (red) loose packing, (green) dense packing.

2.2.1 Volume Fraction Measurement by Surface Laser Scan

With the use of a height laser sensor mounted on a computer-controlled translation stage, the one dimensional surface profile of the packing can be recorded, see figure 2.7-B. Such a scan takes approximately two minutes.

Figure 2.6 illustrates the scanning control (as well as the shaking process). The whole scanning process is operated by a computer. The surface profile in one direction of the ellipsoid packing can be scanned by a laser sensor. A translation stage driven by a stepper motor is used to move the laser sensor across the surface. The stepper motor is connected to a stepper drive (geckodrive G210). A labjack U6 interface, which is connected via USB to the computer, triggers the gecodrive controller. The provided exodriver for python and C++ is used to communicate with the labjack. The height laser sensor is connected via a serial port - USB adapter to the computer. A C++ program is used to read out the height.

The packing fraction of the jammed ellipsoid configuration in the container can be calculated by two methods. The first one is the scanning method which uses the surface scan and can be done instantaneous. The second method needs tomography and reconstruction. It is described in section 2.7. In the following the first method is described and compared to the tomographic method.

By measuring the average height of the surface profile, the packing fraction of the ellipsoid pack can be calculated as

$$\Phi = \frac{h_0}{h} \tag{2.2}$$

where h is the average height of the surface scan and h_0 is the height of the packing given a packing fraction of 100%. h_0 can be calculated as

$$h_0 = \frac{\sum V_e}{\pi r_{\text{cyl}}^2} \tag{2.3}$$

where the sum is over all volumes V_e of the ellipsoids inside the container and r_{cyl} is the radius of the container. For the monodisperse case, $\sum V_e = N V_e$, where N is the number of ellipsoids in the container.

If h_0 is unknown, $\Phi(h)$ can only be calculated in arbitrary units by choosing an arbitrary h_0.

The error in the measurement of the average height Δh is estimated to be 1mm. The corresponding error in the packing fraction $\Delta\Phi(h)$ can then be calculated as

$$\Delta\Phi(h) = \frac{h_0}{h^2} \cdot \Delta h. \tag{2.4}$$

(Note that the $\Delta\Phi(h) \sim h^{-2}$ dependence reflects the fact that the larger the packing in terms of particle numbers, the smaller the error in the global packing fraction.)

The packing fraction calculated by equation (2.4) from the average height $\Phi(h)$ can be compared to the global packing fraction Φ which was determined by tomography (chapter 2.7). For the calculation of $\Phi(h)$ an arbitrary h_0 is chosen. As expected there
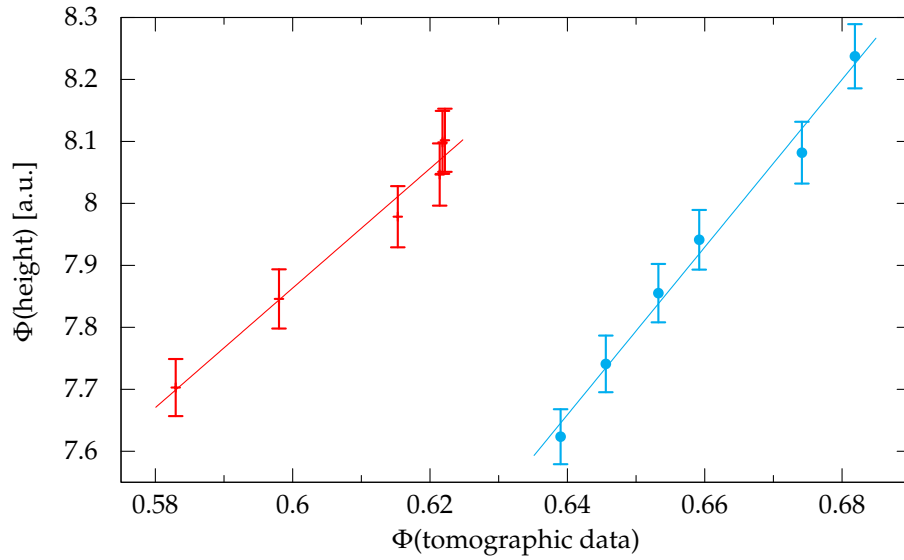
Figure 2.8: Comparison between global packing fraction extracted from the tomographic data and the packing fraction measured by surface scanning for spheres and ellipsoids. $\Phi(h)$ is given in arbitrary units. (red) sphere-like ellipsoids with aspect ratio $\alpha = 0.97$; (blue) ellipsoids with aspect ratio $\alpha = 0.59$.

is a linear dependence between these two methods, see figure 2.8. The total shift between the two aspect ratios is due to the arbitrary h_0 chosen for each aspect ratio. The packing fraction extracted from the tomographic data is only calculated in the middle of the container. Boundary effects at the container wall and a inhomogeneous local packing fraction distribution could cause the small differences from the linear proportionality, seen in figure 2.8.

The more accurate tomographic method can be used calibrate the much faster scanning method. Hence, the average height is a good and relatively fast indicator of the global packing fraction of ellipsoid packings without doing tomography.

2.3 Tomographic Imaging

X-Ray tomography is the reconstruction of 3D spatial structures from X-Ray projections at multiple directions. It is used to obtain high resolution 3D real-space data of the ellipsoid packing. To this end container, prepared by the methods described in section 2.2, is placed into an X-Ray Tomograph (GE Nanotom), see figure 2.9. The current and acceleration voltage of the X-Ray tube are chosen to maximize the contrast between material and air in the resulting image. Table 2.2 shows the values used.

The projections are taken with the option of "detector movement", which means that the detector is moved slightly to the left and to the right for every image to

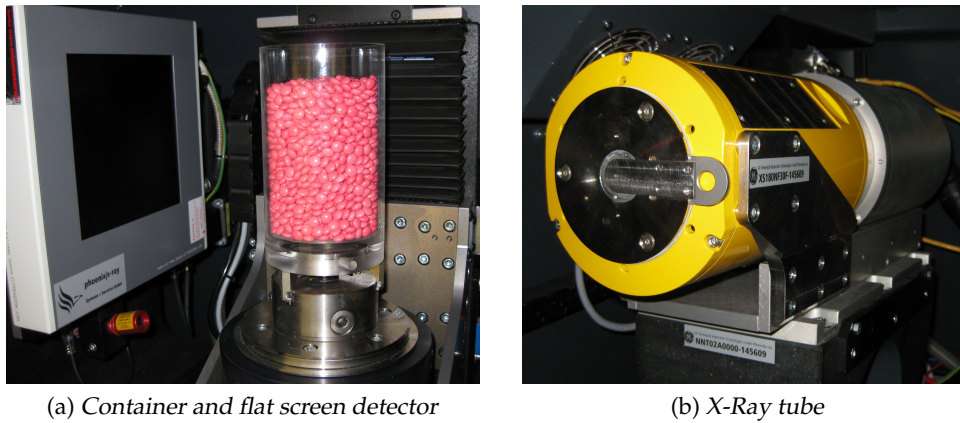(a) *Container and flat screen detector* (b) *X-Ray tube*

Figure 2.9: Components of the "GE Nanotom" commercial X-Ray tomograph system used to gain 3D data of ellipsoid packings.

type	acceleration voltage	current
PPP	120 kV	160 μA
3DP	140 kV	140 μA

Table 2.2: Current and acceleration voltage of the X-Ray tube used for the different particle types. 3DP = 3D printer; PPP = pharmaceutical placebo pill.

reduce the problem of ring artifacts. For containers which exceed the range of the detector, the "tiling option" is used. This option moves the detector at first to the left side and the first half of the image is recorded. Then the detector is moved to right, the right half of the image is recorded and merged with the first half. To be able to merge the images correctly, a small overlap between the images is needed. With this option, images which are larger than the flat screen detector can be recorded. The maximum diameter of a cylindrical container which fits into the Nanotom is 104 mm.

The resulting image is a 3D raster graphics image with cubic volume elements called *voxels*. From the geometry of the setup the resolution of the resulting images can be calculated. The setups used in this work alway result in a resolution of 0.064 mm/voxel according to the Nanotom software.

2.4 Image Processing: From Grayscale to Labeled Images

Starting with a 3D-grayscale image (see figure 2.10) reconstructed from the projections of the X-Ray tomography using the program phoenix datos|x - reconstruction (Version 1.5.0.14), the single ellipsoidal particles in the 3D-grayscale image are detected to get a labeled 3D-image. The algorithm consists in several steps which are explained in the following. The flow diagram in figure 2.13 pictures the parts of the algorithm and its connections. The subsequent segmentation steps are illustrated by the sequence of 2D image slices in figure 2.14. The first slice represents the original grayscale image.
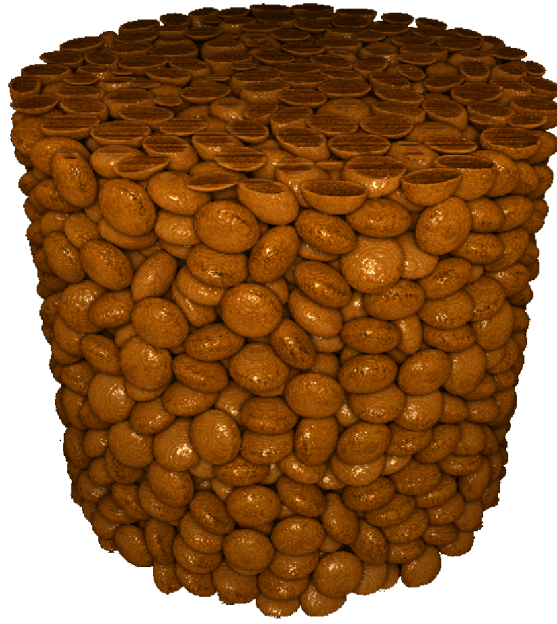
Figure 2.10: Three-dimensional perspective view of an ellipsoid configuration, rendered from the original 3D-grayscale data using the volume rendering tool *Drishti* [41].

For the particle detection algorithm a binary image is needed. The easiest way to binarize a grayscale image is by threshold segmentation with a global threshold G_c, i.e., considering all voxels with gray-value $G < G_c$ as representing the air phase (black) and all others as representing the particle phase (white).

In the reconstructed grayscale images a lower intensity in the center of the container and overexposures at the sides of the container are commonly observed. The rotational symmetry of the cylindrical container means that the intensity variation is radially dependent. Thus, the threshold is varied with the radius, as a global threshold will not give good results.

To make the image a binary image, the gray-value histograms of different radial layers R_i are calculated and analyzed, see figure 2.11-A. The two peaks in each of the bimodal histograms represent the material and the air phase, see figure 2.11-B. To get the best separation, the threshold for each layer is chosen in the minimum between the two peaks. For each distance R_i the threshold can be extracted. The threshold function $G_c(r)$ is defined as the linear interpolation between these extracted thresholds, see figure 2.12.

The threshold for each linear distance can be calculated and the grayscale image can be binarized by the following rule:

$$\text{If}(G < G_c(r)) : \text{Voxel is set to black (air phase)}$$
$$\text{If}(G \geq G_c(r)) : \text{Voxel is set to white (ellipsoid phase)} \quad (2.5)$$

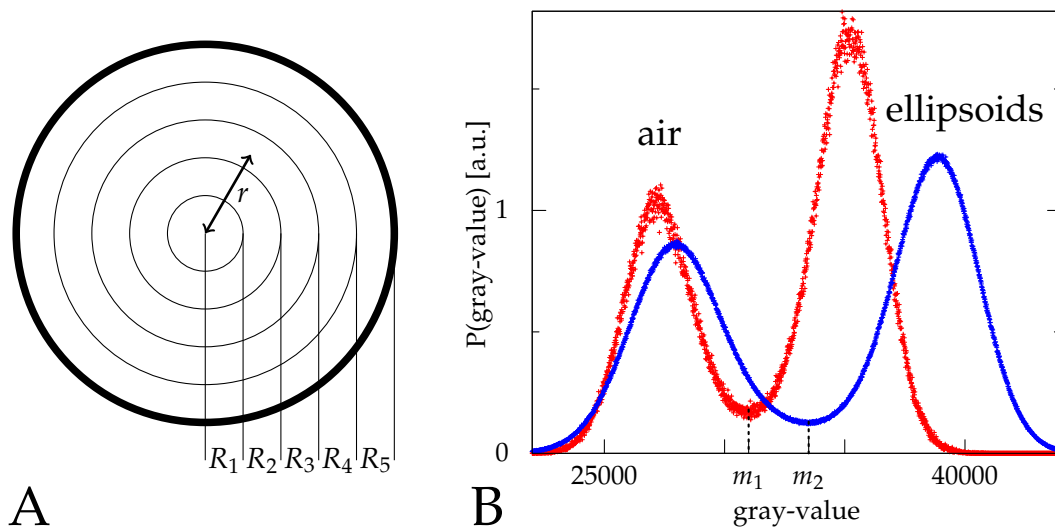A slice of the resulting binary image can be seen in figure 2.14b.

Figure 2.11: Determination of the radial threshold function $G_c(r)$ used for gray-scale image segmentation: (**A**) sketch of top view of the cylindrical container, the radial layers R_1 to R_5 are illustrated. (**B**) gray-value histogram for two different layers: (red) layer near center, (blue) layer near side of container. The minima of the two curves are marked with m_1 and m_2.
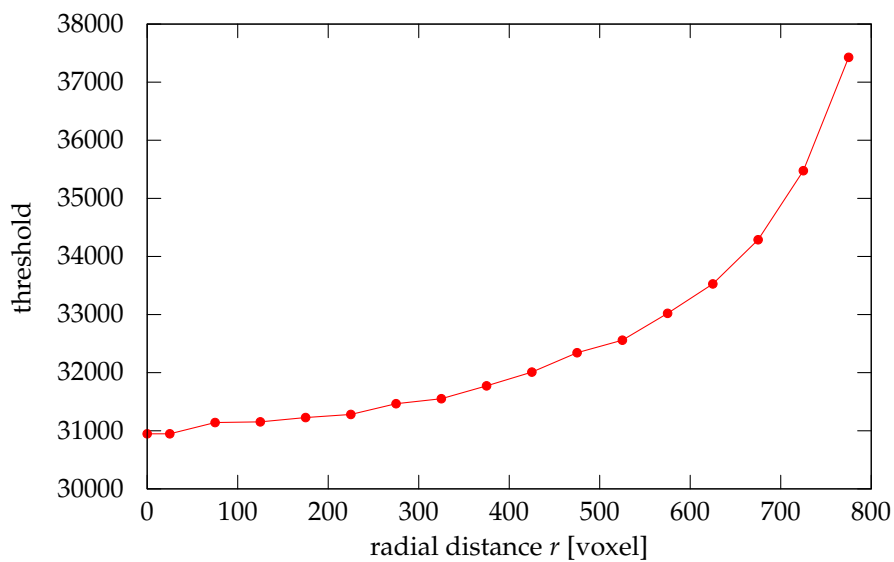

Figure 2.12: Radial threshold dependence $G_c(r)$ for gray-scale image segmentation with linear interpolation between the steps, see also figure 2.11.
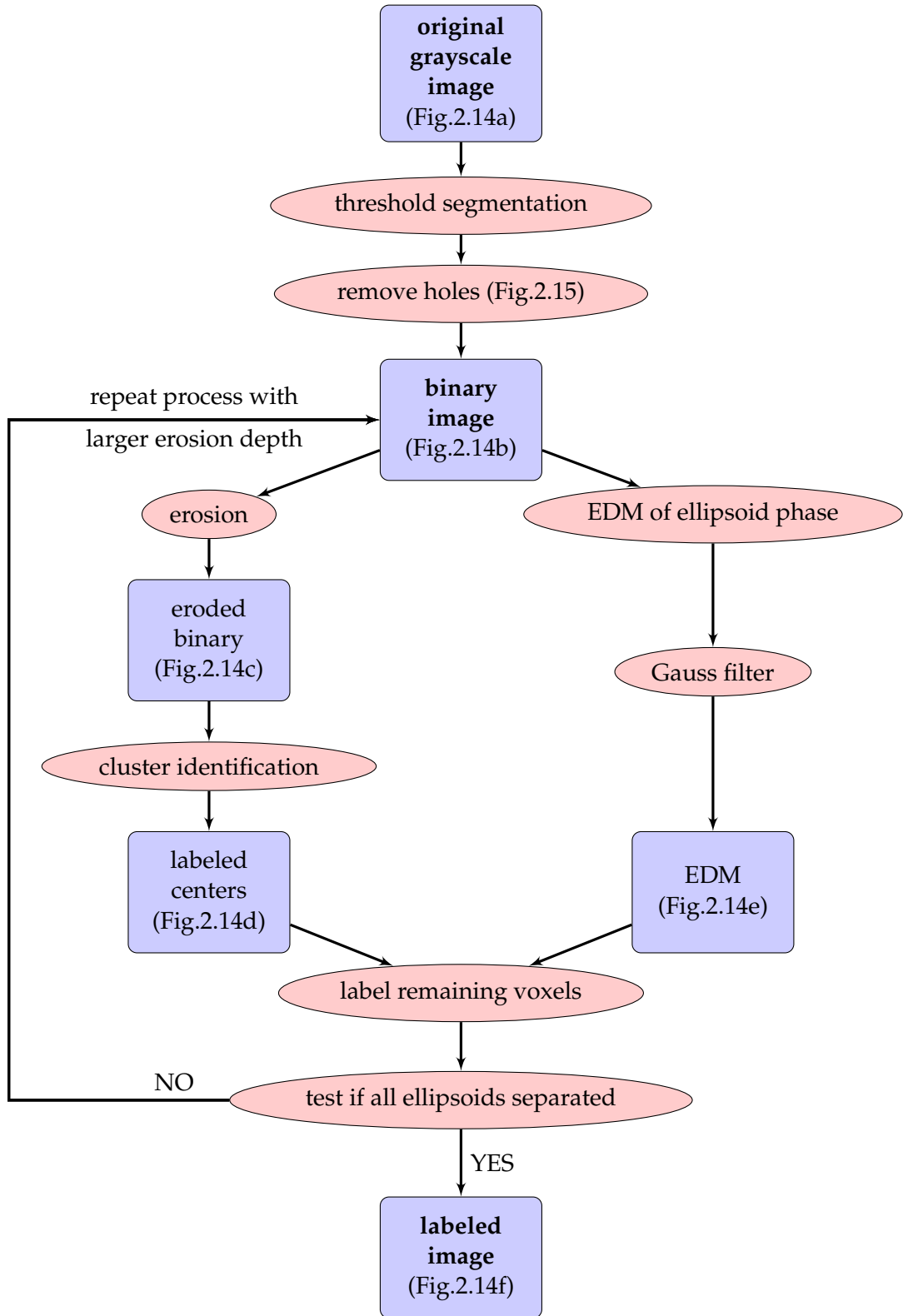
Figure 2.13: Flow diagram of segmentation algorithm. Elliptical nodes describe the segmentation steps and rectangular ones resulting data/images types. Examples of the different intermediate steps are shown in figure 2.14.
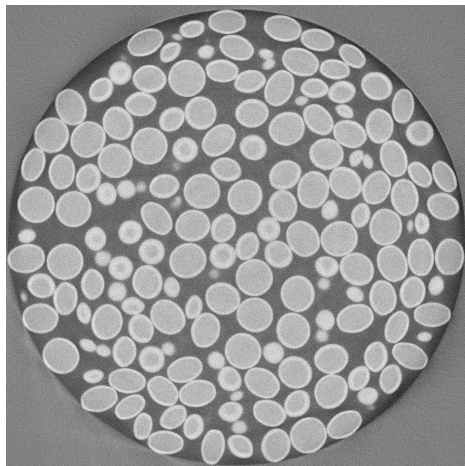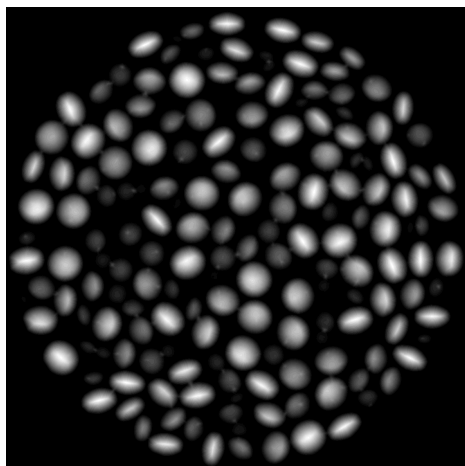
(a) *Original grayscale image slice*
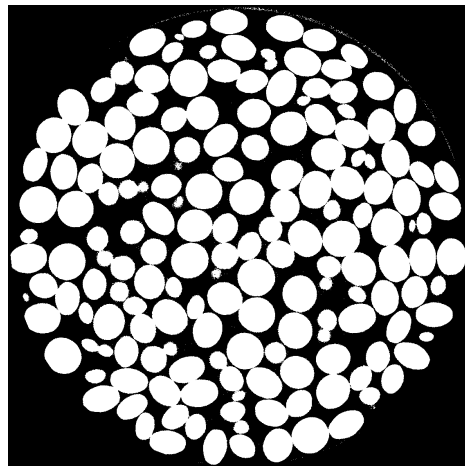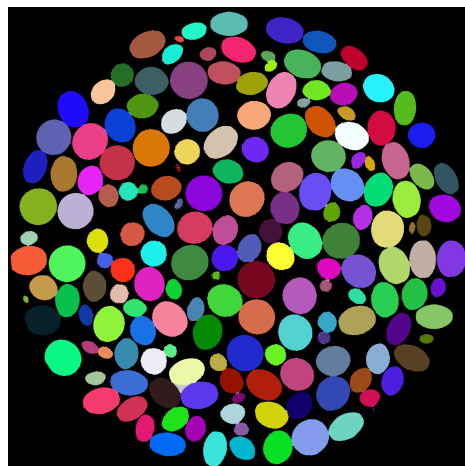
(b) *Thresholded image*
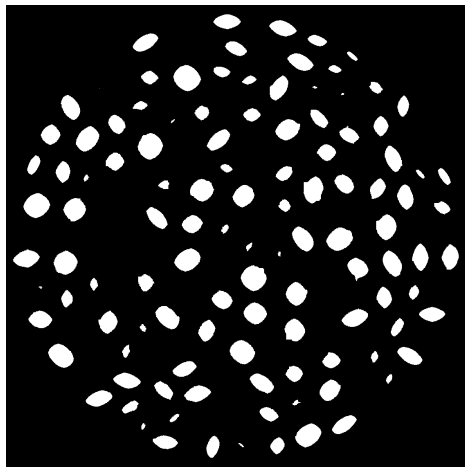
(c) *eroded binary*

(d) *labeled eroded binary*

(e) *EDM of binary image*

(f) *binarized & labeled ellipsoids*

Figure 2.14: Intermediate steps of the particle detection algorithm described in the flow diagram in figure 2.13.
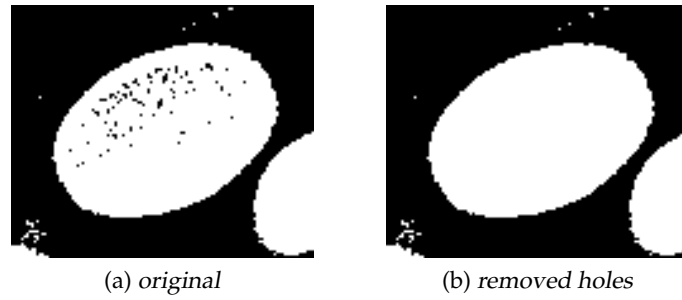
(a) *original*   (b) *removed holes*

Figure 2.15: Isolated cluster removal: Binary image slices of an ellipsoid before and after removing "isolated clusters". The isolated cluster removal step is necessary, becaues small cluster of spurious "air" voxels can remain inside the ellipsoids after the threshold segmentation.

Isolated cluster removal

In the white ellipsoids of the binary image, often some spurious black voxels remain. Image 2.15a shows a close-up image of a single ellipsoid. For the separation process describe below, these wrongly identified voxels have to be eliminated. To remove these holes, the Hoshen Kopelmann cluster identification algorithm [63] is used to identify all black clusters. The biggest cluster is the real air phase surrounding the particles and stays black. All the other small clusters are set to white because they represent falsely identified black voxels, which can be caused, for example, by air bubbles in the particles. The result of this step can be seen in figure 2.15b.

In some cases spurious clusters are not removed, because they are connected to the air phase. This problem is solved by varying the threshold with the radius, see figure 2.12. In some rare cases, this error still occurs for a very small number of individual ellipsoids (typically not more than one per dataset). If this happens, these ellipsoids need to be separated manually together with their neighborhood, segmented and inserted back into the 3D image.

Identification of the ellipsoids

After the creation of the binary image, the actual identification of the ellipsoids begins. At first the white phase of the image is eroded. The erosion ϵ_R of the phase X of a binary image with radius R is defined by

$$\epsilon_R(X) = \{\mathbf{x} \mid B_R(\mathbf{x}) \subseteq X\} \qquad (2.6)$$

with the sphere $B_R(\mathbf{x})$ of radius R and center $\mathbf{x}$ [81].

A very effective method to calculate the eroded image, is by thresholding the Euclidean distance map (EDM) of the ellipsoid phase [31]. The EDM of the white phase of a binary image labels each voxel with the distance to the nearest black voxel. It can be calculated by solving a minimization problem [20].

The erosion depth has to be chosen such that all ellipsoids become separated. Table 2.3 shows the used erosion depth for each aspect ratio.

type	aspect ratio	short half-axis	long half-axis	erosion depth
3DP	1.00	47 voxels	48 voxels	16 voxels
3DP	0.91	46 voxels	51 voxels	15 voxels
3DP	0.71	39 voxels	54 voxels	16 voxels
PPP	0.64	30 voxels	47 voxels	13 voxels
3DP	0.60	34 voxels	58 voxels	15 voxels
PPP	0.59	32 voxels	55 voxels	15 voxels
3DP	0.40	25 voxels	61 voxels	17 voxels

Table 2.3: Erosion depth and spatial resolution for each particle type (3DP = 3D printer; PPP = pharmaceutical placebo pill).

After the erosion step, all ellipsoids should be separated, as shown in figure 2.14c (If not all ellipsoids are separated, which can be determined in the end, the segmentation has to be done again with a larger erosion depth, see below). The remaining parts can again be labeled and counted with the Hoshen Kopelmann algorithm [63], see figure 2.14d. The number of clusters of the eroded image is the number of ellipsoids in the analyzed part of the cylinder.

The voxels, which were previously eroded, also need to be labeled. For this step an EDM of the original binary image is needed. A slice of the EDM is pictured in figure 2.14e. To avoid unwanted artifacts in the next step, the EDM is smoothed by a Gauss filter. All white (ellipsoid) voxels that are not yet labeled (those that were eroded in the previous step) are now connected to the neighboring voxel, indicated by the gradient of the EDM. Now the connections are resolved: If a voxel is already labeled, all connected voxels are labeled equivalently. White voxels that remain unlabeled after this step are ignored: they are treated as wrongly identified white voxels that do not belong to an ellipsoid.

Every cluster should represent one ellipsoid and hence all clusters should have approximately the same size in the end, corresponding roughly to the small degree of polydispersity of the particles. If the variation in cluster size is larger than compatible with the particle polydispersity, some ellipsoids have not been separated properly by the erosion. In this case the segmentation process is repeated, for the whole sample, with a larger erosion depth. The final result of the particle detection is shown in figure 2.14f.

2.5 Extraction of Ellipsoid Shape Features from Labeled Images

In the last section a labeled image of the tomographic data was generated. This section describes the extraction of the shape features (position, orientation, size) of ellipsoids from such labeled images. For the analysis of the ellipsoid packings, the defining features of the single ellipsoids in the ensemble are needed. An ellipsoid is described by:

- its center point: $\mathbf{c}$

- its three normalized axis vectors: $\mathbf{a}_1, \mathbf{a}_2, \mathbf{a}_3$

- its three half-axis lengths: e_1, e_2, e_3

Figure 2.16 pictures an ellipsoid and its defining features. The following sections describe the calculation of these defining features from a segmented 3D-picture.
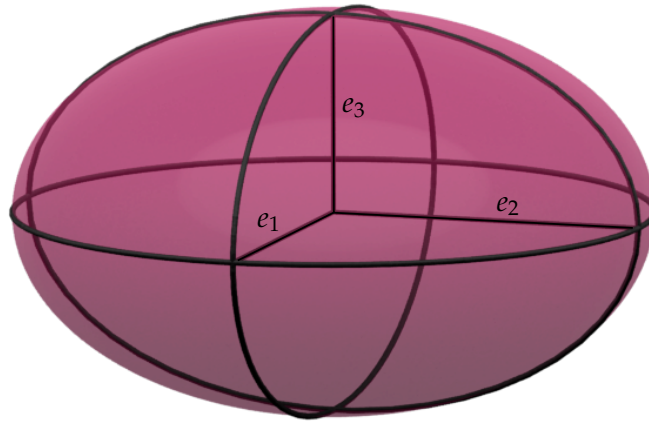
Figure 2.16: Ellipsoid and its defining features. e_1, e_2 and e_3 are the lengths of three half-axis.

2.5.1 Minkowski Tensors of Binary and Labeled Images

This chapter describes the calculation of the following Minkowski tensors for binary images:

- W_0, a scalar representing the volume of the considered object.

- $\mathbf{W}_0^{1,0}$, a vector which is the center of mass multiplied by the volume of the object.

- $\mathbf{W}_0^{2,0}$, a tensor which quantifies the distribution of mass within the object. It is related to the tensor of inertia.

The exact definition and geometric interpretation of the Minkowski tensors has already been described in chapter 1.4.1.

In the following calculations, a binary image with a black phase (represents air) and a white phase (represents ellipsoids) is assumed. The Minkowski tensors of the white phase are calculated. The defining features of a voxelized ellipsoid can be extracted of the three above mentioned tensors, see chapter 2.5.2. Images with labeled objects (e.g. labeled image of an ellipsoid packing, see section 2.4) can be treated as binary images for every label, hence the calculation for each label is the same as for a binary image.

W_0 represents the volume of the white phase. Hence, the voxels of the white phase are summed up.

$\mathbf{W_0^{1,0}}$ can be interpreted as the center of mass multiplied by the volume and can be calculated for binary images as follows:

$$\mathbf{W_0^{1,0}}(\text{ellipsoid}) = \sum_{\text{white voxels}} \begin{pmatrix} x \\ y \\ z \end{pmatrix}_{\text{voxel}} \tag{2.7}$$

For the calculation of $\mathbf{W_0^{2,0}}$ the calculation of the same tensor for a unit cube with center in the origin U_0 is needed.

$$\mathbf{W_0^{2,0}}(U_0) = \begin{pmatrix} \frac{1}{12} & 0 & 0 \\ 0 & \frac{1}{12} & 0 \\ 0 & 0 & \frac{1}{12} \end{pmatrix} \tag{2.8}$$

The translation of the Minkowski tensors is given by

$$\mathbf{W_\nu^{r,s}}(K \uplus \mathbf{t}) = \sum_{p=0}^{r} \binom{r}{p} \mathbf{t}^p \, \mathbf{W_\nu^{r-p,s}}(K) \tag{2.9}$$

where the body K translated by a vector $\mathbf{t}$ is denoted $K \uplus \mathbf{t}$ [74]. Thus, the tensor $\mathbf{W_0^{2,0}}$ of the unit cube with center in the origin translates as

$$\mathbf{W_0^{2,0}}(U_0 \uplus \mathbf{t}) = \mathbf{W_0^{2,0}}(U_0) + \mathbf{t} \otimes \mathbf{t} \tag{2.10}$$

with the tensor product $\otimes$. As the Minkowski tensors are additive (see section 1.4), $\mathbf{W_0^{2,0}}$ of the white phase is the summation of $\mathbf{W_0^{2,0}}$ (w.r.t. the same common origin) of each white voxel.

2.5.2 Extraction of Ellipsoid Properties from Minkowski Tensors

The defining features of an ellipsoid can be extracted from the Minkowski tensors W_0, $\mathbf{W_0^{1,0}}$ and $\mathbf{W_0^{2,0}}$, whose calculation was explained in the previous section. For an ensemble of ellipsoids it is important that the Minkowski tensors are all calculated with respect to the same origin.

The center of mass vector $\mathbf{c}$, can be represented by W_0 and $\mathbf{W_0^{1,0}}$ as follows:

$$\mathbf{c} = \frac{\mathbf{W_0^{1,0}}}{W_0} \tag{2.11}$$

The axis vectors $\mathbf{a}_1, \mathbf{a}_2, \mathbf{a}_3$ are given by the eigenvectors of $\mathbf{W}_0^{2,0}$.
For the calculation of the aspect ratio, at first, an axis-aligned ellipsoid in the Cartesian coordinate system is assumed. An axis-aligned ellipsoid can be transformed to a sphere by the following linear transformation:

$$\mathbf{r}' = \begin{pmatrix} \frac{1}{a} & 0 & 0 \\ 0 & \frac{1}{b} & 0 \\ 0 & 0 & \frac{1}{c} \end{pmatrix} \mathbf{r} = \mathbf{G}\mathbf{r} \tag{2.12}$$

For a sphere $\mathbf{W}_0^{2,0}$, can be calculated exactly [74].
$\mathbf{W}_0^{2,0}$ of an ellipsoidal particle K can then be calculated as

$$
\begin{aligned}
\mathbf{W}_0^{2,0} &= \int_K (\mathbf{r} \otimes \mathbf{r}) \, \mathrm{d}^3 r \\
&= \int_{\mathbb{S}_2} \left(\mathbf{G}^{-1} \mathbf{r}' \right) \otimes \left(\mathbf{G}^{-1} \mathbf{r}' \right) \frac{1}{\det \mathbf{G}} \, \mathrm{d}^3 r' \\
&= \mathbf{G}^{-1} \underbrace{\left(\int_{\mathbb{S}_2} \mathbf{r}' \otimes \mathbf{r}' \, \mathrm{d}^3 r' \right)}_{\frac{4\pi}{15} \mathbb{1}} abc \cdot \mathbf{G}^{-1} \\
&= \frac{4\pi}{15} abc \cdot \mathbf{G}^{-1} \mathbb{1} \mathbf{G}^{-1} \\
&= \frac{4\pi}{15} abc \begin{pmatrix} a^2 & 0 & 0 \\ 0 & b^2 & 0 \\ 0 & 0 & c^2 \end{pmatrix}
\end{aligned}
\tag{2.13}
$$

with the unit sphere $\mathbb{S}_2$ and the three-dimensional unit matrix $\mathbb{1}$.
Considering now an arbitrary ellipsoid, the aspect ratios α_1 and α_2 can be extracted from the eigenvalues λ_1, λ_2 and λ_3 of $\mathbf{W}_0^{2,0}$, if the ellipsoid is placed in the origin, by the following equations:

$$\alpha_1 := \frac{e_1}{e_2} = \sqrt{\lambda_1/\lambda_2} \tag{2.14}$$

$$\alpha_2 := \frac{e_1}{e_3} = \sqrt{\lambda_1/\lambda_3} \tag{2.15}$$

For the absolute axis lengths, W_0 or the volume also has to be considered. The volume V of an ellipsoid is given by

$$V = W_0 = \frac{4}{3}\pi \cdot e_1 \cdot e_2 \cdot e_3 \tag{2.16}$$

$$= \frac{4}{3}\pi \cdot e_1 \cdot \frac{e_1}{\alpha_1} \cdot \frac{e_1}{\alpha_2} \tag{2.17}$$

The axis length e_1 can then be calculated as:

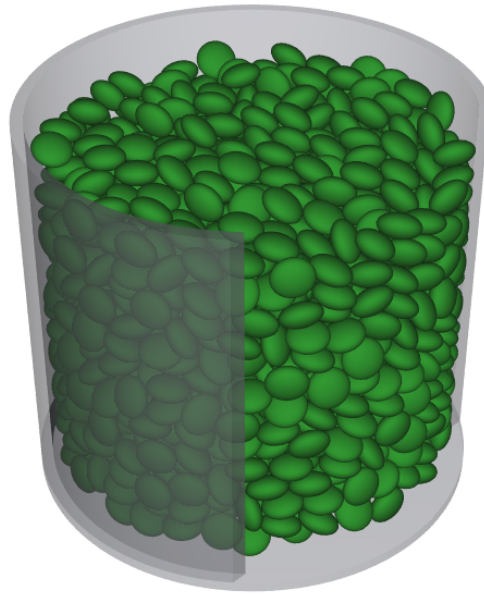$$e_1 = \sqrt[3]{\frac{3 \cdot V \cdot \alpha_1 \cdot \alpha_2}{4 \cdot \pi}} \tag{2.18}$$

Figure 2.17: Rendered 3D image of an ellipsoid packing in a cylindrical container used the rendering tool povray (`www.povray.org`). In contrast to figure 2.10, this image is based on a set of ellipsoids placed at the center points and orientations as extracted from the tomographic image.

and then e_2 and e_3 can be calculated very easily from equations (2.14) and (2.15).

With all this information, the position, orientation and size of the ellipsoids of a labeled image can be reconstructed. Figure 2.17 shows a 3D image of detected ellipsoids in a cylindrical container.

2.6 Contact Numbers

A very simple topological quantity of granular packings is the average contact number, i.e. the average number of neighbors in contact with an objects. As any interaction and force is transmitted from particle to particle through mutual contacts, the contact number is conceptually a very important parameter for the mechanical stability of a packing. Therefore, the contact number of jammed ensembles is a well-studied parameter in the literature [5, 9, 14, 55, 80]. However, the contact number is highly sensitive to details of its definition, due to its discrete values.

For experimental data, the contact numbers are hard to determine, because the contact number is a discontinuous function of the particle positions and their orientations. The finite accuracy of the X-Ray tomography and the reconstruction as well as deviations of experimental particle shape from perfect ellipsoids lead to small deviations in position and orientations. Hence, a simple geometric "contact counting" would lead to incorrect contact numbers. The polydispersity of the particles does

not affect the determination of the contact number, because the analysis in this thesis treats the ellipsoids as polydisperse objects.

To determine the average contact number of an ellipsoid ensemble, an algorithm is needed to decide whether two given ellipsoids intersect or not.

2.6.1 Intersection of Ellipsoids

An ellipsoid can be defined by

$$K(\mathbf{r}) := \left(\frac{(\mathbf{a}_1 \cdot (\mathbf{r} - \mathbf{c}))^2}{e_1^2} + \frac{(\mathbf{a}_2 \cdot (\mathbf{r} - \mathbf{c}))^2}{e_2^2} + \frac{(\mathbf{a}_3 \cdot (\mathbf{r} - \mathbf{c}))^2}{e_3^2} \right) - 1 = 0 \qquad (2.19)$$

The test if two ellipsoids (K_1 and K_2) intersect can be formulated as a constrained minimization, which can be solved by the method of Lagrange multipliers: Minimize $K_2(\mathbf{r})$ subject to the constraint $K_1(\mathbf{r}) = 0$ [69]. This can be written as:

$$\min F(\mathbf{r}, \lambda) \quad \text{with} \quad F(\mathbf{r}, \lambda) = K_2(\mathbf{r}) - \lambda K_1(\mathbf{r}) \qquad (2.20)$$

At the Minimum, the first derivative is zero.

$$\frac{\partial F}{\partial r_i} = 0 \quad , \quad i = 1,2,3 \qquad (2.21)$$

$$\frac{\partial F}{\partial \lambda} = 0 \qquad (2.22)$$

This system of equations can be solved by Newton's method [63]. Newton's method can be used to find the roots of these 4 equations for the derivations $\frac{\partial F}{\partial r_i}$ and $\frac{\partial F}{\partial \lambda}$. These roots correspond to minima or maxima of the distance function for points of K_1 to K_2. In order to converge to the minimum, the starting point has to be set in the half of the ellipsoid K_1, which is closer to ellipsoid K_2, otherwise Newton's method converges to the maximum. The starting point is set to

$$\mathbf{r}_{\text{start}} = \frac{1}{2} \cdot (\mathbf{c}_1 + \mathbf{c}_2) \qquad (2.23)$$

$$\lambda = 0 \qquad (2.24)$$

with the two center points of the ellipsoids $\mathbf{c}_1$ and $\mathbf{c}_2$. After a few steps Newton's method converges to $\mathbf{r}_{\text{final}}$, the minimum on ellipsoid K_1. The position of $\mathbf{r}_{\text{final}}$ determines if the ellipsoids intersect or not. If $K_2(\mathbf{r}_{\text{final}}) > 0$, the ellipsoids don't intersect because $\mathbf{r}_{\text{final}}$ lies outside ellipsoid K_2. Otherwise the ellipsoids intersect.

2.6.2 Determining the Average Contact Number

In order to extract the average contact number k from the tomographic data, the method introduced by Aste *et al.* for spheres [5] is improved and generalized for ellipsoids. A morphological scaling factor of the ellipsoids x is introduced for this method. The scaling factor x dilates the ellipsoids with a sphere B_s of radius s, where

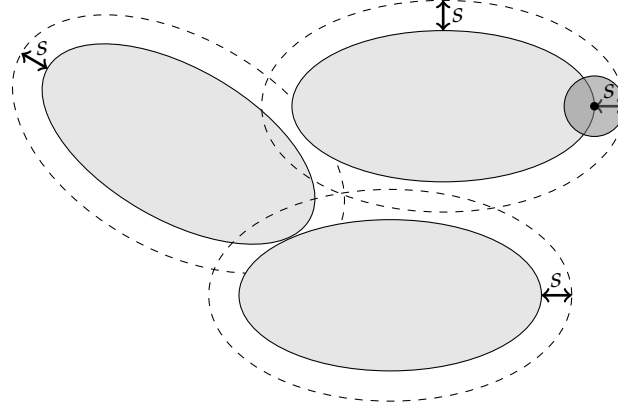$$s = x \cdot \sqrt[3]{\frac{3V_{av}}{4\pi}} \qquad (2.25)$$

Figure 2.18: Morphological dilation of the ellipsoids by a sphere of radius *s*. As the dilation radius is increased, a larger number of nearby ellipsoids are identified as "in contact". The approach of section 2.6 to identify the correct contact number relies on guessing the correct form of the CNS function and fitting the data to this curve.

and V_{av} is the average Volume of the ellipsoids in the ensemble. A negative x leads to an erosion of the ellipsoids. The dilation $K(e_1, e_2, e_3) \uplus B_s$ of an ellipsoid $K(e_1, e_2, e_3) = \{(x,y,z) | \frac{x^2}{e_1^2} + \frac{y^2}{e_2^2} + \frac{z^2}{e_3^2} \leq 1\}$ with half-axes e_1, e_2, e_3 is different from the larger ellipsoid $K(e_1 + s, e_2 + s, e_3 + s)$ with half-axes $e_1 + s$, $e_2 + s$, $e_3 + s$.[1] However, for small s, $K(e_1 + s, e_2 + s, e_3 + s)$ is a good approximation of the dilation $K(e_1, e_2, e_3) \uplus B_s$. An illustration can be seen in figure 2.18.

Contact number scaling function

The average contact number of an ellipsoid ensemble can be extracted from a contact number scaling function (CNS function). The CNS function maps the morphological scaling factor x onto the average contact number of the ensemble. The CNS function is a sum of two parts $f_1(x)$ and $f_2(x)$.

The first part of this sum $f_1(x)$ is represented by a step function convoluted with a Gauss function. To understand this part, exact data of jammed hard ellipsoids is assumed where no ellipsoids overlap and each ellipsoid touches with its neighbors at one point. In this case, if the dilated ellipsoids are smaller than their actual size (for $x < b$) there should be no contacts. When the ellipsoids reach their actual size (for $x = b$), the function jumps to the average contact number a of the ensemble. The morphological scaling factor at this point is denoted by b. Hence, for exact data the first part of the CNS function can be described by a step function $h(x)$.

$$h(x) = a \cdot \theta(x - b) \tag{2.26}$$

---

[1] Note that this dilation operation corresponds directly to the inverse of the erosion operation used in equation 2.6 for the identification of the ellipsoids.

(The second part of the sum $f_2(x)$, relevant for the gradually increasing number of contact when the ellipsoids are dilated beyond their original size for $x > b$, is dealt with below).

For experimental data, the position, size and orientation of the ellipsoids are not exact, there are small deviations due to the tomography and reconstruction. These errors are assumed to be distributed Gaussian and represented by the Gauss function $g(x)$.

$$g(x) = \frac{c}{\sqrt{\pi}} e^{-(c \cdot x)^2} \quad , \quad \sigma = \frac{1}{\sqrt{2}c} \tag{2.27}$$

The width of the Gauss function is denoted by σ.

The first summand of the CNS function for experimental data can be calculated as the convolution of the step function $h(x)$ and the Gauss function $g(x)$:

$$f_1(x) = h(x) * g(x)$$

$$= \int_{-\infty}^{\infty} h(x) \cdot g(y - x) \mathrm{d}x$$

$$= \int_{-\infty}^{\infty} g(x) \cdot h(y - x) \mathrm{d}x$$

$$= \frac{a \cdot c}{\sqrt{\pi}} \int_{-\infty}^{\infty} e^{-(c \cdot x)^2} \cdot \theta(y - x - b) \mathrm{d}x$$

$$= \frac{a \cdot c}{\sqrt{\pi}} \int_{-\infty}^{y-b} e^{-(c \cdot x)^2} \mathrm{d}x$$

$$= \frac{a \cdot c}{\sqrt{\pi}} \underbrace{\int_{-\infty}^{0} e^{-(c \cdot x)^2} \mathrm{d}x}_{\frac{\sqrt{\pi}}{2c}} + \frac{a \cdot c}{\sqrt{\pi}} \underbrace{\int_{0}^{y-b} e^{-(c \cdot x)^2} \mathrm{d}x}_{\frac{\sqrt{\pi}}{2c} \mathrm{erf}\,(c\,(x-b))}$$

$$= \frac{a}{2} + \frac{a}{2} \mathrm{erf}\,(c\,(x - b)) \tag{2.28}$$

with the error function:

$$\mathrm{erf}\,(x) = \frac{2}{\sqrt{\pi}} \int_{0}^{x} e^{-\tau^2} \mathrm{d}\tau \tag{2.29}$$

Now for the second part: When the ellipsoids are dilated beyond their original size ($x > b$), ellipsoids which have no physical contact but are close to each other are now in contact. This increase of the CNS function with x is, by lack of deeper insight, assumed to be a linear function $f_2(x)$. The function $f_2(x)$ starts at the inflection point of the error function, and is defined by:

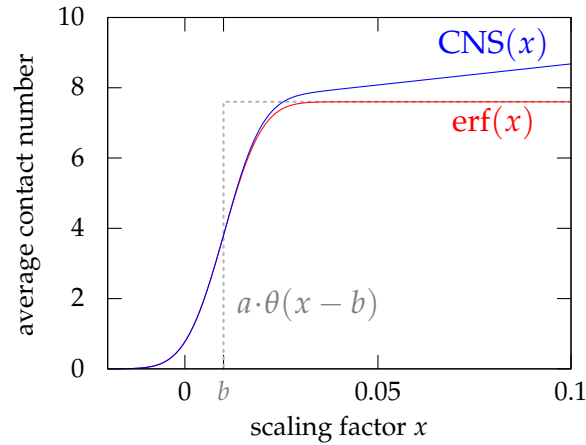$$f_2(x) = \theta(x - b) \cdot d \cdot (x - b) \tag{2.30}$$

Figure 2.19: Model of the fitted contact number scaling (CNS) function to extract the average contact number from tomographic data; (blue) CNS function, (red) error function, (dashed) step function.

The size of the ellipsoids at the inflection point b is the actual size of the ellipsoids.

The combined CNS function for the analysis of the tomographic data is the sum of the convolution of $h(x)$ and $g(x)$ (equation (2.28)) and the linear increase $f_2(x)$:

$$\text{CNS}(x) = \frac{a}{2} \left(1 + \text{erf}\left(c\left(x - b\right)\right)\right) + \theta(x - b) \cdot d \cdot (x - b) \tag{2.31}$$

An illustration of the CNS function can be seen in figure 2.19.

Now the parameters of the CNS function can be tuned to match the data of detected ellipsoids in a tomographic image. With the intersection test of ellipsoids described in section 2.6.1, a discrete CNS function of the detected ellipsoids can be extracted. The implementation of the non-linear least-squares Marquardt–Levenberg algorithm in the gnuplot graphics program (`www.gnuplot.org`) [89] is used to fit the CNS function to the data of the detected ellipsoids. The fitting is done twice: At first, the CNS function is fitted to a large dilation range of the particles, to get first estimates of the parameters. In a second fit, the fit of the CNS function is restricted to the range

$$[b - 4\sigma : b + 8\sigma] \tag{2.32}$$

The width of the error function σ can be calculated from c (see equation (2.27)). For the definition of the fit-range, the parameters b and c are taken from the first fit. After the second fit, the fit parameter a represents the average contact number. Figure 2.20 shows the CNS functions fitted to a dataset of placebo pills and to a dataset of 3D-Printer particles. The differences of the fit for the ellipsoids produced by the 3D-printer and the data are due to the small protrusions of the ellipsoids. The larger σ is also caused by the inaccurate shape of these particles and results in a larger fitting range.

The width of the error function σ is a good indicator for the accuracy of the particle shapes. It is also obvious that the larger σ, the larger the ambiguity of the exact

value of the average contact number. At the moment there is no method available to quantify the error of the extracted average contact number. Thus, the contact numbers in the analysis are given without error bars.

Beyond its use to determine average contact numbers, the CNS function is also used to determine the size of the ellipsoids in the tomographic data. For the further analysis of the packing fraction and anisotropy, the ellipsoids are dilated to their actual size indicated by the inflection point of the CNS function.

(a) *Packing of placebo pills.*　　(b) *Packing of of 3D-Printer particles.*
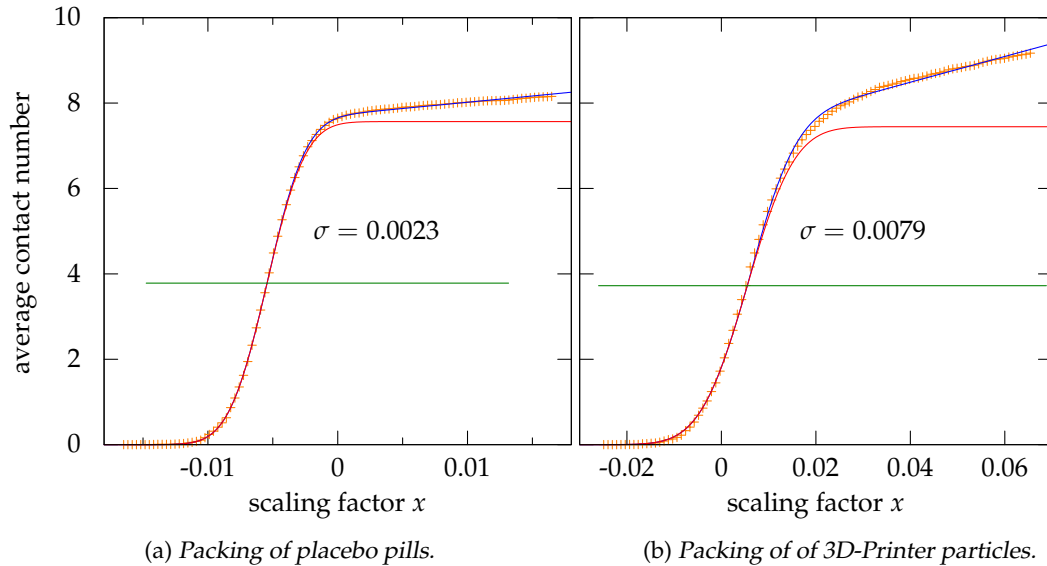
Figure 2.20: Fitting the CNS function to data of detected ellipsoids in a tomographic image to determine the average contact number. The accuracy of the placebo pills is much better than the one of the 3D-Printer particles. This is evident also in the width of the error function, which is much smaller for the placebo pills. The green line indicates the fitting range.

2.7 Generalized Voronoi Diagram for Ellipsoidal Particles

This section describes an algorithm for the calculation of the Set Voronoi diagram for aspherical or polydisperse objects, introduced in section 1.3.

To calculate the set Voronoi diagram, the surface of the ellipsoidal particles is discretized by vertices connected by triangles (surface triangulation), see figure 2.22. The normal (point) Voronoi diagram of all these vertices is calculated using the software tool qhull [8]. The Voronoi diagram of the discretization consists of two types of facets, those that separate two vertices of *the same* ellipsoid, and those that separate two vertices of *different* ellipsoids. The latter represent an approximation of the Set Voronoi diagram of the ellipsoid configuration. The set Voronoi diagram is hence obtained from the normal Voronoi Diagram of the triangulation by removing the
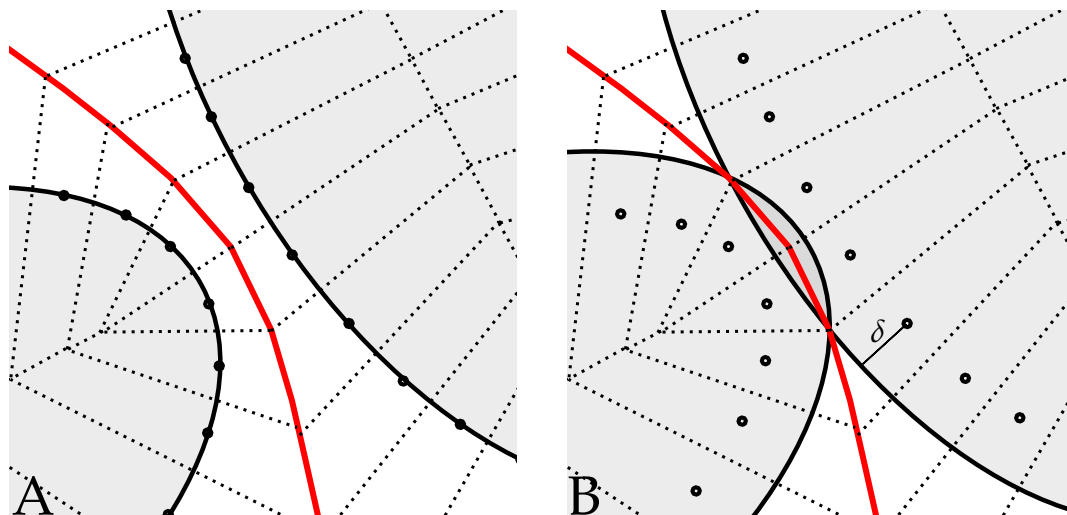
Figure 2.21: Construction of the set Voronoi diagram. (**A**) Set Voronoi diagram of non-overlapping particles (gray) obtained as a subset of the facets of the point Voronoi diagram of a surface triangulation. (**B**) Set Voronoi of overlapping ellipsoids. Prior to the computation of the Set Voronoi diagram, the particles are eroded (by a parallel surface transformation) to eliminate overlap. In both figures the symbols are: (black line) ellipsoid surface; (black dots) discretized parallel surface; (dashed) Voronoi cells of points on discretized parallel surface; (ref) generalized Voronoi cell.

superfluous facets which lie between seed points on the same object. The construction of the generalized Voronoi diagram is illustrated in figure 2.21-A.

This construction of the Set Voronoi diagram provides a good approximation provided that the typical edge length of the surface is small compared to the minimal distance between adjacent objects/ellipsoids (Indeed, while we have not formally pursued this, a convergence analysis similar to the related Voronoi-based Medial axes algorithms [3, 75] appears possible). For ellipsoidal particles in geometric contact, this criterion is not fulfilled. In fact, even worse, due to the accuracy of the reconstruction algorithm, adjacent ellipsoids may have a very slight overlap. Fortunately, the Set Voronoi diagram of an ellipsoid packing is the same as that of the same packing with all ellipsoids (parallelly) eroded by a (not too) large value δ, see Figure 2.21-B. Therefore, the ellipsoidal particles are eroded (points moved along the inwards-pointing surface normal) prior to the computation of the Set Voronoi diagram.

Note that the construction of this generalized Voronoi diagram bears a strong resemblance to the Medial axis or medial surface construction [10, 79] and the described algorithm to the Voronoi-based medial axis algorithm [3, 75].

Assuming that the Set Voronoi cells represent the local volume associated to each particle, the local packing fraction Φ_l for each ellipsoid can be calculated:

$$\Phi_l = \frac{V_{\text{ellipsoid}}}{V_{\text{cell}}} \tag{2.33}$$

The global packing fraction Φ is then defined as the average value of all local packing fractions (over all ellipsoid particles, excluding those close to the container walls).

$$\Phi = \langle \Phi_l \rangle = \frac{\sum \Phi_l}{\#\text{ellipsoids}} \tag{2.34}$$

In the following the technical details of the discretization and the calculation of the generalized Voronoi Cell are described.

Note that, in contrast to the normal point Voronoi diagram, the Voronoi Cells of the Set Voronoi diagram are not necessarily convex, even if the particles are.

Figure 2.23 shows a 3D image of a generalized Voronoi cell of a single ellipsoids of a jammed ellipsoid configuration. In figure 2.14 a slide of segmented ellipsoidal particles in a cylindrical container and an image of the corresponding generalized Voronoi cells of the inner ellipsoids can be seen.

Discretized representation of an ellipsoid and its parallel surface

First, an ellipsoid aligned with the coordinate axes is discretized and the parallel surface (erosion) is calculated. Then the discretized surface is translated and rotated to the position and orientation of the original ellipsoid (as extracted from the tomographic data).

An axis-aligned ellipsoid (aligned with the coordinate axes) can be parameterized by

$$\begin{aligned} x &= e_1 \cos(\varphi) \sin(\theta) \\ y &= e_2 \sin(\varphi) \sin(\theta) \qquad (0 \le \varphi \le 2\pi, 0 \le \theta \le \pi) \\ z &= e_3 \cos(\theta) \end{aligned} \tag{2.35}$$

with the three axis length e_1, e_2 and e_3.

For a homogeneous discretization of a sphere into triangles of (approx) the same size, the surface element

$$\sin(\theta)\mathrm{d}\varphi\mathrm{d}\theta \tag{2.36}$$

of the sphere between the triangulation vertices need to be constant. This constraint is also used for the discretization of the ellipsoid surface, which leads to a higher discretization of regions with high curvature, a somewhat desirable side effect!

At first, the circle of $\theta = \pi/2$ is discretized with N points of equally distance, by using a $\delta\varphi(\theta = \pi/2)$ of $2\pi/N$. Now $\delta\theta$ is chosen as $\delta\varphi(\theta = \pi/2)$. To fulfill the constraint in equation (2.36), $\delta\varphi$ needs to be increased for smaller θ.

$$\delta\varphi(\theta) \propto \frac{1}{\sin(\theta)} \tag{2.37}$$

---

[2]For the image in (b) the generalized Set Voronoi cells are not determined by the triangulated algorithm of section 2.7 but by a voxel-based algorithm. This algorithm generates a water-shed partition of the void space in the ellipsoid configuration, with respect to the Euclidean distance map, similar to ideas in ref. [68].
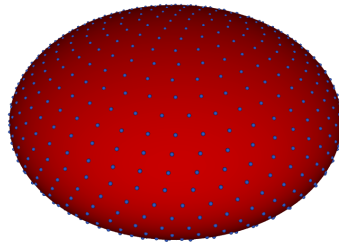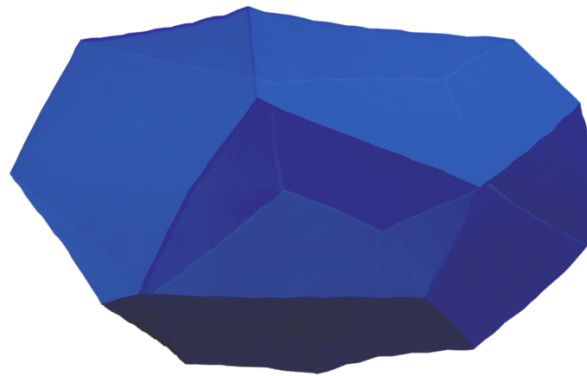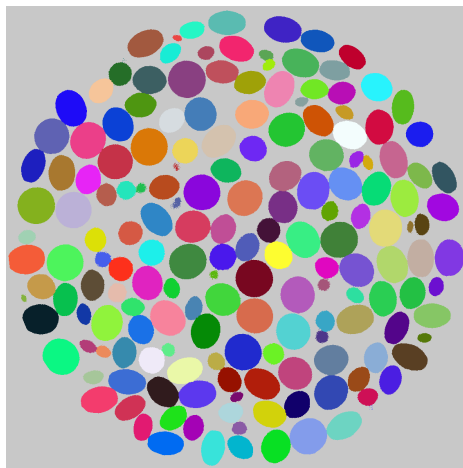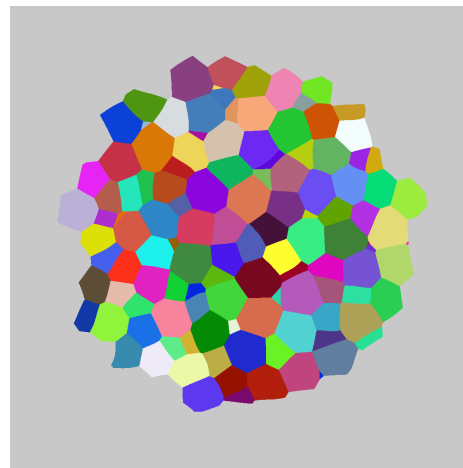
Figure 2.22: Discretized ellipsoid surface.

Figure 2.23: A generalized Voronoi cell of a single ellipsoids of a jammed ellipsoid configuration. Note that the facets of the Set Voronoi diagram can be curved and the cells are not necessarily convex.

(a) *detected ellipsoids*

(b) *generalized Voronoi cells*

Figure 2.24: Image slice of segmented ellipsoidal particles in a cylindrical container and the corresponding generalized Set Voronoi cells[2]. Voronoi cells of the outermost layer of particles near the cylinder wall are not shown, because a closed Voronoi cell is not defined for them.

An example of a discretized ellipsoid surface is illustrated in figure 2.22. Now the points are shifted along the inward-pointing surface normal $n(\theta, \varphi)$, see equation (2.39), to get the discretized parallel surface. For this, the normal vector to the ellipsoid surface is needed. For a point $\mathbf{p}$

$$\mathbf{p} = \begin{pmatrix} e_1 \cos(\varphi) \sin(\theta) \\ e_2 \sin(\varphi) \sin(\theta) \\ e_3 \cos(\theta) \end{pmatrix} \tag{2.38}$$

on the ellipsoid surface, the normal vector to the ellipsoid surface can be calculated as

$$\mathbf{n}(\mathbf{p}) = \frac{\mathrm{d}\mathbf{p}}{\mathrm{d}\varphi} \times \frac{\mathrm{d}\mathbf{p}}{\mathrm{d}\theta} = \begin{pmatrix} e_2 e_3 \cos(\varphi) \sin(\theta) \\ e_1 e_3 \sin(\varphi) \sin(\theta) \\ e_1 e_2 \cos(\theta) \end{pmatrix} \tag{2.39}$$

The discretized parallel surface is the surface defined by the points $\mathbf{p} + \delta \, \mathbf{n}(\mathbf{p})$. In order to retain convexity and a smooth bounding surface of the eroded ellipsoid, the value of δ must not exceed the smallest radius of the curvature, which is

$$r_{\min} = \frac{e_1^2}{e_3} \tag{2.40}$$

with the smallest axis e_1 and the largest axis e_3 [47].

3 Statistical Properties of Ellipsoid Packings

In this chapter the statistical properties extracted from the experimental datasets are discussed. First, the range of global packing fractions that can be explored by the tapping method as well as the spatial distribution of local packing fractions in the resulting configurations are analyzed. Further the orientational alignment of the ellipsoids with the direction of gravity, as function of distance from the cylinder walls, is determined. The key focus of the chapter is the analysis of contact numbers (both global and local) that are discussed in the context of the jamming paradigm. A further analysis of the local contact number gives a deeper insight how the aspect ratio α and the friction coefficient μ affect the contact number. Besides the contact number analysis, the local environment is also characterized by the shape of Voronoi cells. Their shape is quantified by the anisotropy index $\beta_0^{2,0}$ based on Minkowski tensors, which reveals that the Voronoi Cells of sphere-like particles become isotropic with increasing packing fraction, whereas the shape of the Voronoi Cells of ellipsoids with high aspect ratio remains approximately constant. Finally, section 3.6 compares the results to numerical data of Discrete Element Simulations, in particular for the densest and looses random packings, and to unjammed equilibrium ellipsoid ensembles of much lower densities.

3.1 Global Packing Fractions and Compaction

Experimental realizations of ellipsoid configurations are prepared by the protocols described in section 2.2. To achieve packings with different packing fractions for each aspect ratio, a loose packing is prepared. This loose packing of ellipsoidal particles is then tapped with different number of taps of an acceleration of 4g. The number of ellipsoids in the cylindrical container and the resulting number in the tomogram is shown in table 3.1. The table shows also the number of realized configurations and the symbol for each aspect ratio used in the following plots.

For the analysis of the packing fraction of the contact number and of the anisotropy, the ellipsoids near the container wall are not considered in order to reduce boundary effects. Therefore the outside ellipsoids which are closer than 2cm to the container wall are removed. The remaining analyzed number of ellipsoids can also be seen in table 3.1.

Note that the number of particles with aspect ratio $\alpha = 0.91$ and $\alpha = 0.64$ was not enough to fill the whole container. The experiments with these particles were performed with a half filled container.

aspect ratio	symbol	type	approximate number of particles			# of packings (tapping, other)
			cylinder	tomogram	analyzed	
0.97	+	3DP	5000	2300	800	6 , 0
0.91	+	3DP	2500	1600	490	2 , 5
0.74	+	3DP	5000	2200	720	5 , 0
0.64	●	PPP	5000	4100	1400	5 , 5
0.60	+	3DP	5000	2200	700	6 , 0
0.59	●	PPP	5000	2900	880	6 , 3
0.40	+	3DP	5000	2600	800	5 , 0

Table 3.1: Number of ellipsoidal particles in the container, in the tomographic image and analyzed particles after removing the outermost layers. The first number in the last column represents packings prepared by the tapping method, the second one packings prepared with other methods. 3DP = 3D printer; PPP = pharmaceutical placebo pill.

The packing fraction of an ellipsoid packing is adjusted by the tapping procedure described in section 2.2. By tapping the container, the height of the packing gets smaller which means that the packing gets denser. This dependence is also recognized by the analysis of the global packing fraction in the tomographic image, see figure 3.1. The increase in density by tapping the container and the reach of constant packing fraction for large number of taps is consistent with published results [62, 67]. Ellipsoids seem to behave in the same way, but it takes longer to reach a constant packing fraction. This can be explained with the elongation. Spheres move more easily because they have rotational symmetry in all directions. The more ellipsoidal its shape, the harder it is for a particle to move to the perfect packing position, because it also needs to rotate.

Placebo pills form denser packings than the 3D-Printer particles. The reason is the different friction coefficient μ of the two particle types. The particles of the 3D-Printer have a higher friction coefficient which leads to looser packs because they are more sticky. The placebo pills with a lower friction coefficient μ form denser packs because the particles can slide more easily into denser configurations.

3.2 Local Packing Fractions

Using the generalized Voronoi Diagram of section 2.7 to define a sphere's local volume, the local packing fraction Φ_l (ellipsoid volume divided through Voronoi cell volume) for each single ellipsoid can be defined, see chapter 2.7. An important result is that the distribution of the local packing fraction $P(\Phi_l)$ seems to be largely independent of the aspect ratio α. Distributions of different aspect ratio with global packing fraction of about 0.65 are shown in Figure 3.2. To analyze this behavior for all different packings, the standard deviation of the local packing fraction distribution $\sigma(P(\Phi_l))$ is calculated. It can be seen, the standard deviation depends only on the global packing fraction and not on the aspect ratio α of the ellipsoids, see figure 3.3.
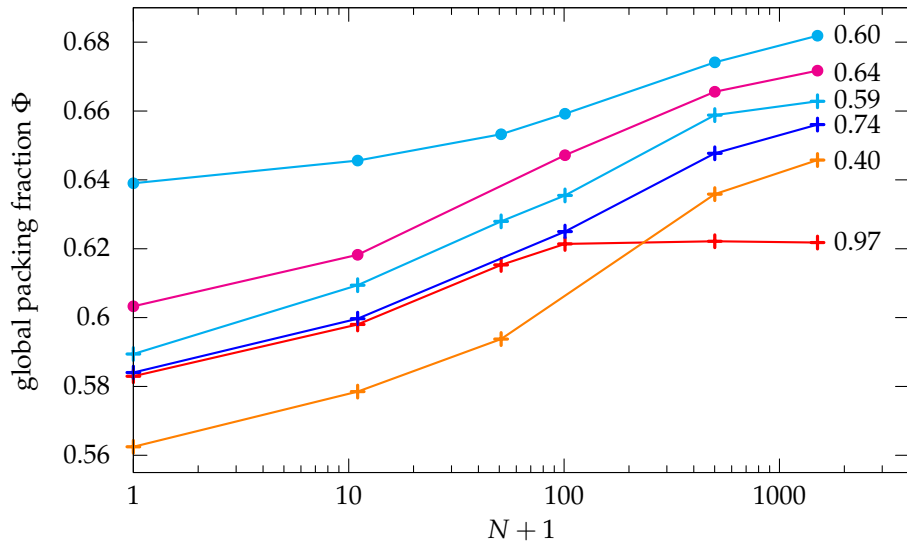
Figure 3.1: Compaction of ellipsoid packings by tapping *N*-times with an acceleration of 4g; the global packing fraction Φ is extracted from the tomographic data. Each curve represents ellipsoids with different aspect ratio *α*, as indicated by the curve labels. (dot) pharmaceutical placebo pills; (cross) 3D-Printer particles.
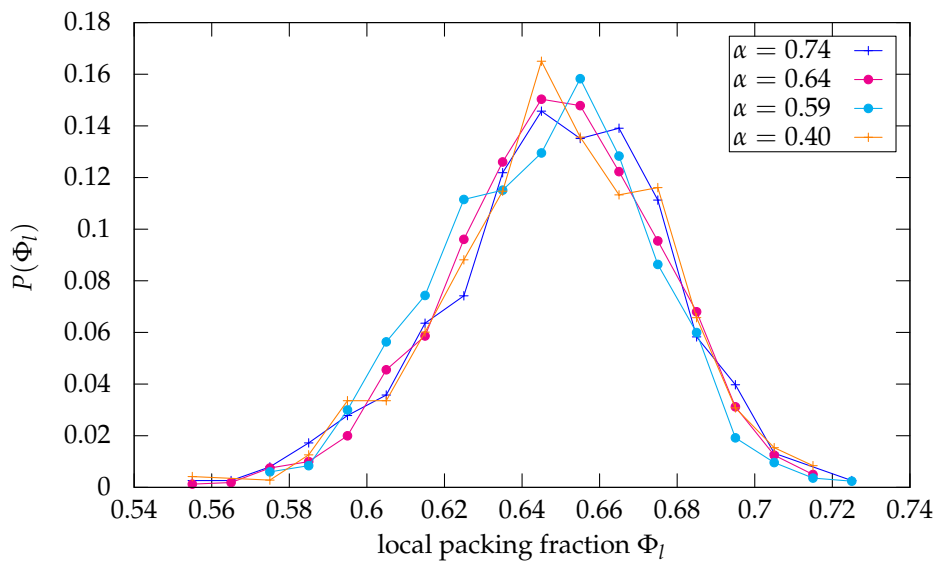

Figure 3.2: Histogram of local packing fractions for different aspect ratios. The global packing fraction for each packing is approximately 0.65. (dot) pharmaceutical placebo pills; (cross) 3D-Printer particles.
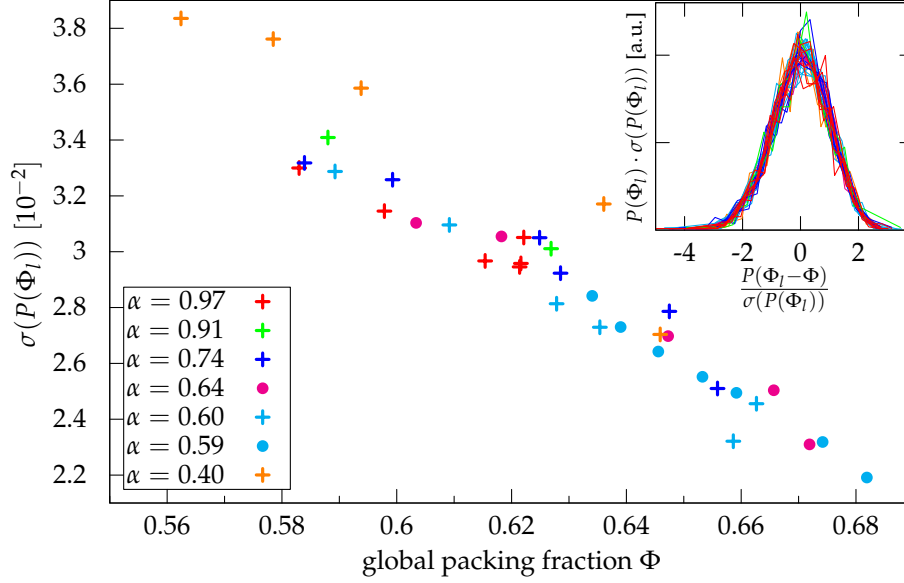
Figure 3.3: Standard deviations of the local packing fraction distributions. The deviations of the ellipsoids with aspect ratio $\alpha = 0.40$ are probably connected to the more inhomogeneous radial packing fraction distribution, see figure 3.4. (dot) pharmaceutical placebo pills; (cross) 3D-Printer particles. The inset shows rescaled local packing fraction distributions of all the ellipsoid packings. The global packing fraction Φ is the average value of all local packing fractions Φ_l.

The inset in figure 3.3 shows rescaled local packing fraction distributions of all the ellipsoid packings, which are lying on top of each other. The global packing fraction Φ is the average value of all local packing fractions Φ_l .

For some configurations of ellipsoids with aspect ratio $\alpha = 0.40$, the standard deviation differs. These deviations are probably connected to spatial inhomogeneities of the packing fraction for these particular configuration, see figure 3.4. This effect needs further investigation with more experimental datasets.

Spatial homogeneity of the packing fraction

Here, the radial and vertical variations of the local packing fractions Φ_l of the particles in the container is discussed. For this analysis all ellipsoids in the tomogram are used, except the outermost layer near the container wall, because a closed Voronoi Cell is not defined for them. The variation of the radial packing fraction is different for the different ellipsoidal particles and aspect ratios, see left panel of figure 3.4. For most of the particles, the packing fraction varies in a range of $\pm 1\%$. The small variations are probably caused by the preparation method with the cardboard tube explained in section 2.2.

The particles with aspect ratio $\alpha = 0.40$ show a trend to a higher packing fraction in the middle of the container ($r = 0$). This inhomogeneity probably causes the
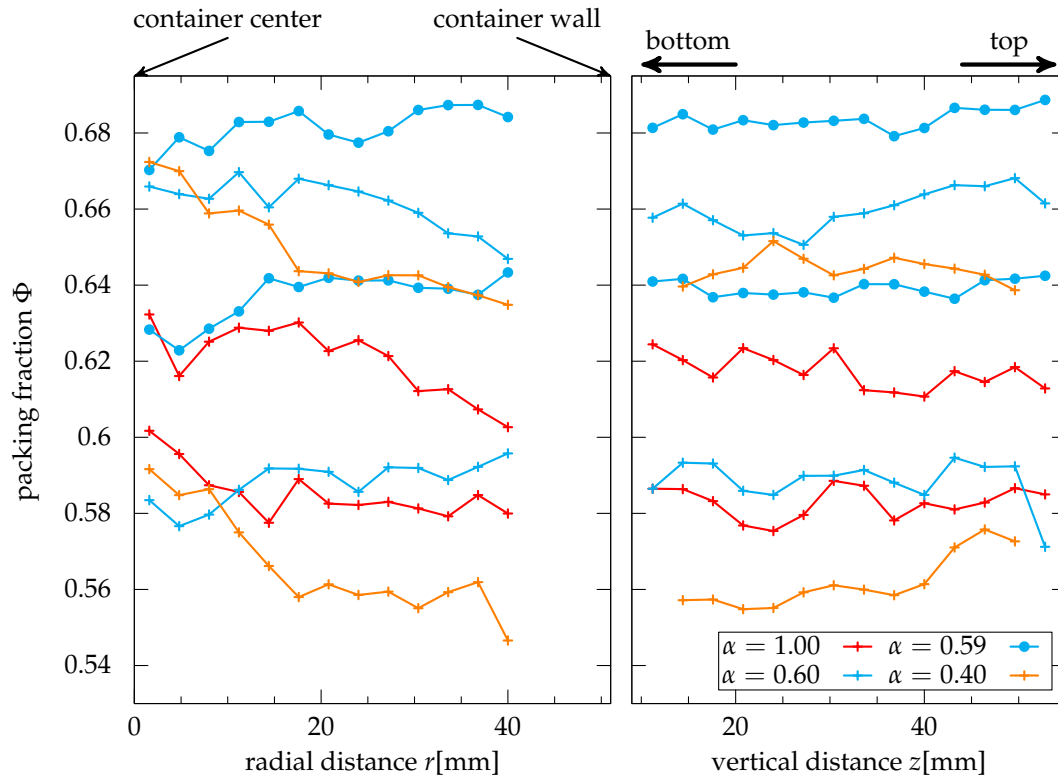
Figure 3.4: Spatial variation of the local packing fraction for a loose and a dense packing of different aspect ratios. The approximate size of the ellipsoidal particles is about 6.5 mm, the exact values are shown in table 2.1. The average packing fraction is the packing fraction averaged over radial or height intervals of approximately 4 mm. *Left panel:* Radial distribution of the packing fraction. *r* is the radial distance from the center of the container. *Right panel:* Packing fraction distribution in vertical direction. (dot) pharmaceutical placebo pills; (cross) 3D-Printer particles.

larger standard deviation of local packing fraction distribution, seen in figure 3.3. The influence of the preparation method and the container wall on the inhomogeneity of the packing fraction distribution needs further investigations.

In the vertical direction the packing fraction stays constant, despite the gravity effects in this direction, see figure 3.4 right panel. The weight of the upper layers on the lower ones has no effect on the vertical packing fraction distribution.

3.3 Orientation

This section quantifies the degree of alignment of the vertical axis $\mathbf{e}_z$ and the average orientation of the particles in the container. The orientation of an oblate ellipsoid can be characterized by the vector of the smallest axis. It is evident that a single oblate ellipsoids (two large, one small axis) on a flat substrate under the action of gravity adopts a particular equilibrium position (with the shorter axis perpendicular to the substrate). To what degree packings of many ellipsoids are influenced by such preferred orientations is the question addressed in this section.

Because of the radial symmetry of the system, the angle between the horizontal coordinate axes is expected to be (and indeed is) random. However, alignment with the vertical axis $\mathbf{e}_z$ is possible.

The polar angle θ_i for an ellipsoid is defined as the angle between the vertical axis $\mathbf{e}_z$ and the orientation axis $\mathbf{e}_s$ of the ellipsoid.
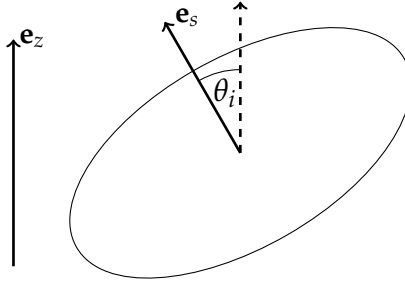
Figure 3.5: Definition of the polar angle θ_i of an ellipsoid.

The average polar angle θ of all ellipsoids is an indicator for the global alignment of the ellipsoids. Figure 3.6 shows the average polar angle for all the different packings.

For a random distribution of vectors on the upper unit sphere half, the average polar angle is

$$\theta_{\text{rand}} = \int\limits_{0}^{90°} \theta \sin(\theta)\ \mathrm{d}\theta = \frac{180°}{\pi} \approx 57° \tag{3.1}$$

Ensembles with $\theta < \theta_{\text{rand}}$ have a preferred alignment with the vertical axis. For ensembles with $\theta > \theta_{\text{rand}}$ the ellipsoids tend to be oriented in the horizontal plane.

By pouring the ellipsoids into the cylinder, oblate ellipsoids orient preferentially in the vertical direction due to gravity. The more ellipsoidal the particles, the stronger is the orientation. It can also be seen, that the orientation decreases with the friction coefficient. The placebo pills with aspect ratio $\alpha = 0.59$ show the strongest degree of alignment. This is probably due to the low friction coefficient. They are also heavier than the placebo pills with aspect ratio $\alpha = 0.64$ which leads to a increased alignment during the preparation process because of gravity.

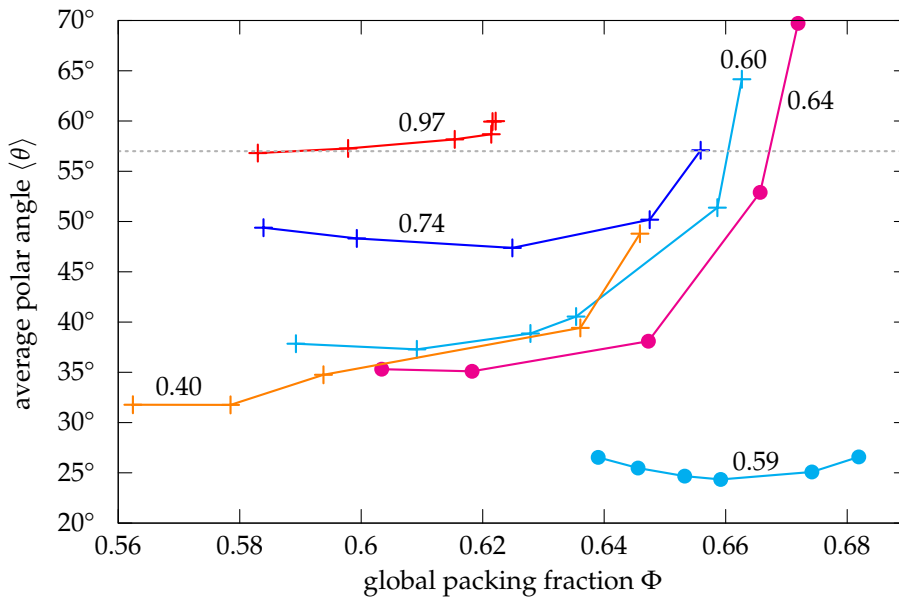By tapping the cylinder, the average angle increases implying that the ellipsoids are distributed more randomly.

Figure 3.6: Global average polar angle of the particles in ellipsoid packings with different global packing fractions Φ and aspect ratios α. The definition of the polar angle is illustrated in figure 3.5. The dashed line indicates the value expected for a fully random distribution of orientations on the unit sphere $\mathbb{S}_2$. The numbers indicate the aspect ratio α of the particles. (dot) pharmaceutical placebo pills; (cross) 3D-Printer particles.

3.4 Analysis of Contact Numbers

3.4.1 Global Contact Number

For each jammed ellipsoid configuration the average contact number can be determined with the "contact number scaling function" method described in Section 2.6. Here the average contact number as a function of the global packing fraction is analyzed. The predominant determinant of the average contact number is the global packing fraction. This can be seen in figure 3.7, where the average contact number as a function of the global packing fraction is shown. The contact numbers are only calculated in the middle of the container, excluding the outermost layers. Ellipsoids closer than 2 cm to the container wall are ignored to reduce boundary effects of the container wall, see section 3.1

Upon closer inspection of the data, differences between the different particles' shapes and friction properties can be resolved. An important result is that at a given packing fraction sphere-like particles have on average less contacts than ellipsoidal ones. Also particles of the same aspect ratio but different friction coefficients seem to behave slightly differently. This can be seen by comparing the placebo pills with aspect ratio $\alpha = 0.59$ to the 3D-Printer particles with almost the same $\alpha = 0.60$, but very different friction coefficient μ.
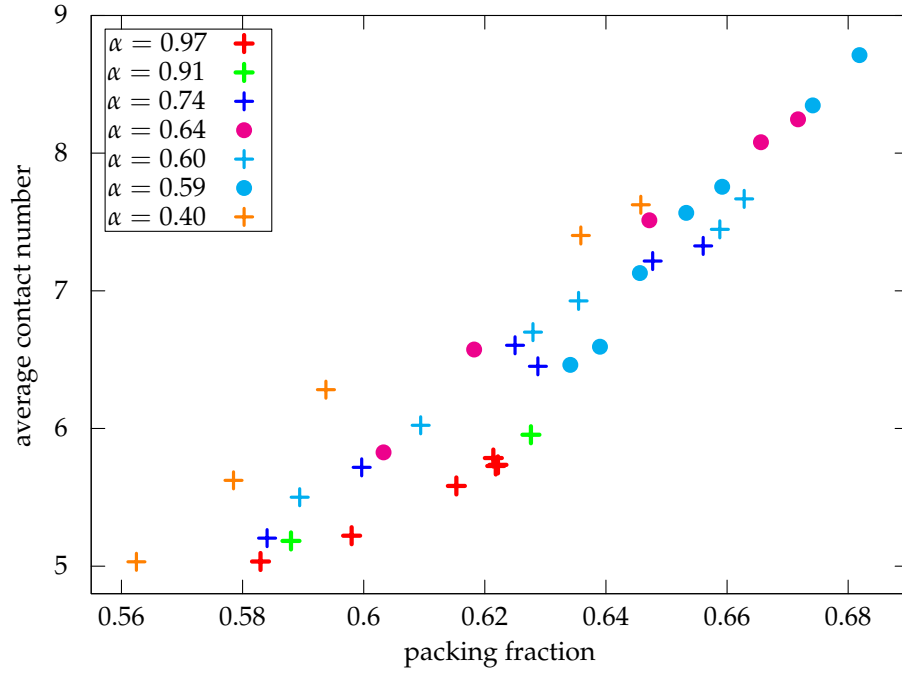
Figure 3.7: Average contact number as a function of the global packing fraction. In first order the points seem to collapse to a master curve, but in second order there are differences. This differences could be caused by the aspect ratio, the friction coefficient and the history. (dot) pharmaceutical placebo pills; (cross) 3D-Printer particles.

The isostatic contact number z_{iso} for frictionless ellipsoidal particles is 4, see section 1.2. It can be observed that the frictional ellipsoid packings are *hyperstatic*, i.e. have more contact than the isostaticity condition requires, see figure 3.7. This is in contrast to packings of frictionless ellipsoids, which are hypostatic (contact number $< z_{iso}$) [16].

In the following, the effect of the aspect ratio α and the friction coefficient μ on the contact number is analyzed.

3.4.2 Local Contact Number

The local contact number for each ellipsoid can also be determined with the same method of section 2.6. This allows an analysis of the local contact number as a function of the local packing fraction Φ_l.

The actual size of the ellipsoids can be determined with the contact number scaling function. Each ellipsoid is dilated to its actual size and a simple geometric contact counting for each ellipsoid determines its number of contacts. The contact number is a discontinuous function and small deviations of the position and orientation lead to errors, see section 2.6. Thus, only the contact number averaged over ellipsoids with the same local packing fraction is compared.
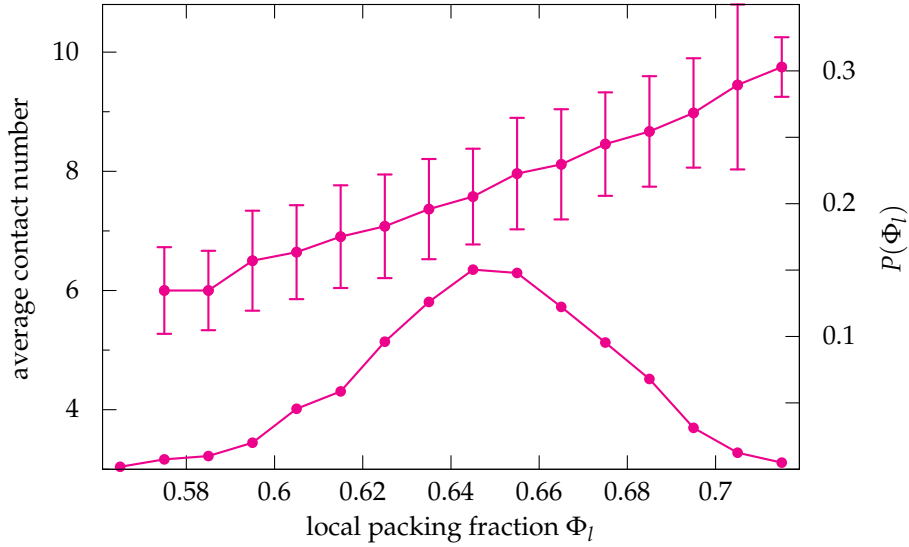
Figure 3.8: Relationship between local packing fraction Φ_l and contact number. At the bottom (and using the right hand scale) the distribution of the local packing fraction of a jammed ensemble with ellipsoids of aspect ratio 0.64 is plotted. The top data points with error bars, represent the contact number averaged over all ellipsoids with local packing fraction between $\Phi_l - 0.005$ and $\Phi_l + 0.005$, using the left hand scale. The error bars represent the width of the distributions of the contact numbers.

Figure 3.8 shows the local packing fraction distribution (using the right hand scale) for a jammed ellipsoid ensemble with global packing fraction 0.648 and ellipsoids of aspect ratio 0.64. On top of the local packing fraction distribution, the contact number averaged over all ellipsoids with local packing fraction between $\Phi_l - 0.005$ and $\Phi_l + 0.005$ (using the left hand scale) is shown. The error bars represent the width of the distributions of the contact numbers. The plot shows, that the average contact number of an ellipsoid increases with the local packing fraction. This seems reasonable as the denser the packing is, the closer the particles are to each other and hence, the more particles are in touch.

Dependence on aspect ratio

The behavior of the local contact number is now compared for spheres and ellipsoidal particles. At first the most sphere-like ($\alpha = 0.97$) and the most oblate particles ($\alpha = 0.40$) both produced with the 3D-Printer are compared. These particles have same friction coefficient but different aspect ratios.

It can be seen, that for sphere-like particles, the local contact numbers are independent of the global packing fraction. The curves coincide, which is in agreement to published results [6]. The small variations are due to the small difference to an exact sphere and poor statistics of approximately 800 analyzed particles per dataset. For ellipsoidal particles it can be observed that these curves split up. The local contact
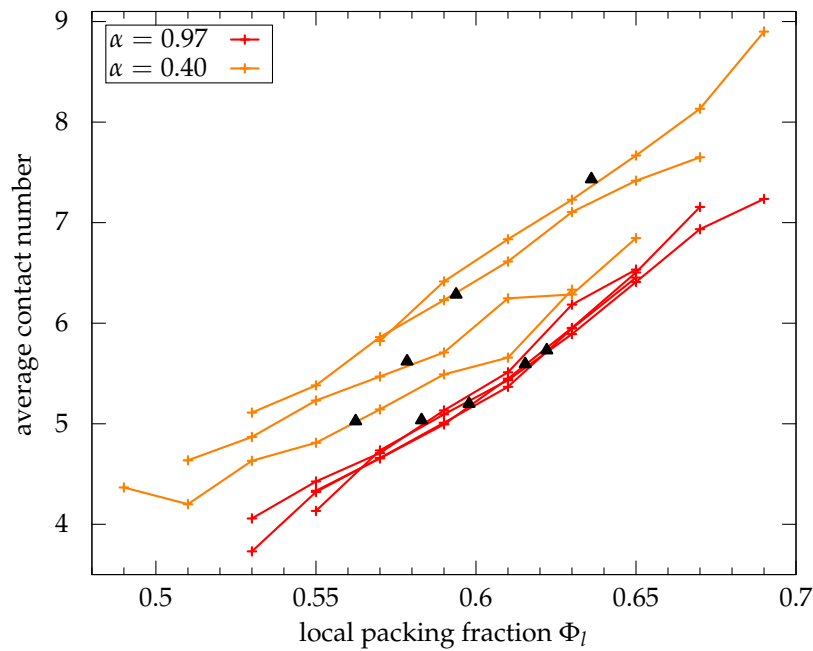
Figure 3.9: Relationship between local packing fraction Φ_l and local contact number for almost spherical and strongly ellipsoidal particles of the same friction coefficient, both produced with the 3D-Printer. For each aspect ratio the curves of the local contact numbers for different global packing fractions are shown. The triangles indicate the global packing fraction and global contact number of the different packings. For the sphere-like particles the curved coincident. Ellipsoidal particles show a vertical offset between the curves.

numbers for denser packs are higher than the ones for looser packs. This split could not be caused by the orientational alignment, the alignment with the vertical axis is the same for three of the shown curves of particles with $\alpha = 0.40$, see section 3.3. By analyzing the curves of more different aspect ratios it can be observed, that the splitting gets stronger the more ellipsoidal the particles are.

The global contact numbers are also represented in these curves by black triangles, see figure 3.9. It can be observed, that the global contact numbers fall onto the local contact number curves. The analysis of the local contact number gives a deeper insight into the contact distribution of ellipsoid packs.

Dependence on friction coefficient

Packings with ellipsoids of approximately the same aspect ratio but different friction coefficient μ are analyzed. Packings of placebo pills with a low friction coefficient are compared to particles of the 3D-Printer with a high friction coefficient, see figure 3.10. Each curve represents a packing with a different global packing fraction. The packings with placebo pills have a smaller range of packing fractions ($\Phi_l = 0.590 - 0.663$) than
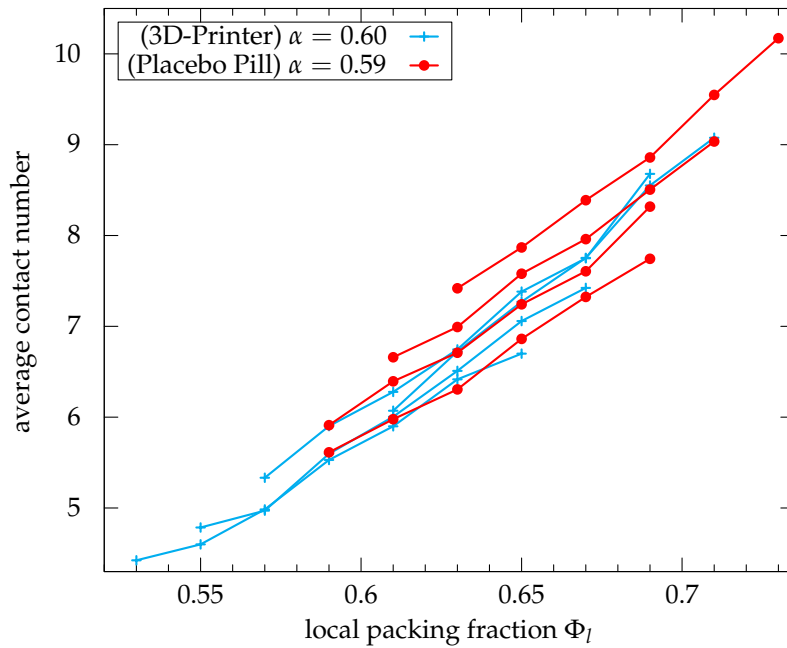
Figure 3.10: Relationship between local packing fraction Φ_l and local contact num-
ber for ellipsoidal particles of different friction coefficient. Each curve
represents the local contact numbers of a packing with a different global
packing fraction Φ. A different range in the vertical splitting for particles
with approximately the same aspect ratio but different friction coefficient
can be observed. (*In this plot, the color of the placebo pill symbols is changed
in order to distinguish more clearly between the curves.*)

the packings with particles fabricated with the 3D-Printer ($\Phi_l = 0.635 - 0.682$).

The local contact number curves of packings with placebo pills are strongly shifted
for different global packing fractions. In contrast, The 3D-Printer particles show only
a small vertical shift between the curves despite them covering a larger range of
global packing fractions.

The different range of the vertical split of the local contact number curves for
particles with approximately the same aspect ratio but different friction coefficient is
a strong indication that the packing properties of ellipsoids depend on the friction
coefficient.

3.5 Anisotropy Analysis of the Particles' Voronoi Cells

The contact number is a local quantity of an ellipsoid and its touching neighbors. Contact numbers are sensitive to the position and orientation of the ellipsoids because of their discontinuous nature with respect to these parameters. Shape measures of Voronoi cells are a further approach to local structure characterization. These geometric (rather than topological) order metrics change continuously with the position and orientation of the particles in contrast to the contact number. Thus, shape measures of Voronoi cells are a good method to describe local quantities of experimental packings, where small inaccuracies of position and orientation occur due to tomography and reconstruction. Here, the characterization of the generalized Set Voronoi cells is done with the anisotropy index $\beta_0^{2,0} \in [0,1]$ based on Minkowski Tensor $\mathbf{W}_0^{2,0}$ eigenvalue ratios, see section1.4. The Minkowski tensor $\mathbf{W}_0^{2,0}$ quantifies the distribution of mass within a solid Voronoi cell and the corresponding anisotropy index $\beta_0^{2,0}$ the deviations from an isotropic cell. For an isotropic packing $\langle \beta_0^{2,0} \rangle$ is 1. The smaller the value of $\langle \beta_0^{2,0} \rangle$, the more anisotropic is the packing. This method was already used to characterize various ensembles of spherical particles [38, 77].

The average anisotropy index $\langle \beta_0^{2,0} \rangle$ as a function of the global packing fraction is analyzed for the experimental packings prepared with the vertical tapping method described in section 2.2. It can be seen in figure 3.11. In addition, packings prepared with a range of different (less well documented) methods and container sizes are shown. These data blend in perfectly with to the ones prepared with the tapping protocol.

For ensembles of jammed spheres $\langle \beta_0^{2,0} \rangle$ increases with the packing fraction, i.e. the packing becomes more isotropic. This behavior was already observed before [77], and is reproduced for the 3D printed sphere-like particles in our experiments.

A new result is that for ellipsoidal particles the behavior changes. For example for packings of ellipsoids with aspect ratio $\alpha = 0.40$ the average anisotropy is approximately constant and independent on the global packing fraction, see the orange line in figure 3.11.

To analyze this change in behavior, linear fits for each aspect ratio α are applied to the data, see lines in figure 3.11. The slope s

$$s = \frac{\mathrm{d}\langle \beta_0^{2,0} \rangle}{\mathrm{d}\Phi} \tag{3.2}$$

of each fit can be analyzed as a function of the aspect ratio, see figure 3.12. For sphere-like particles the slope s is quite high as already known before. Ellipsoidal particles show a much lower (if any) slope s. There must be a transition or cross-over between these two types of behavior. To determine the exact dependence of the slope s on the aspect ratio, packings with more aspect ratios in this range need to be analyzed. Also the friction coefficient has to be considered. The slope s of the placebo pills (dots) is higher than the one of the 3D-Printer particles with roughly the same aspect ratios, see figure 3.12.
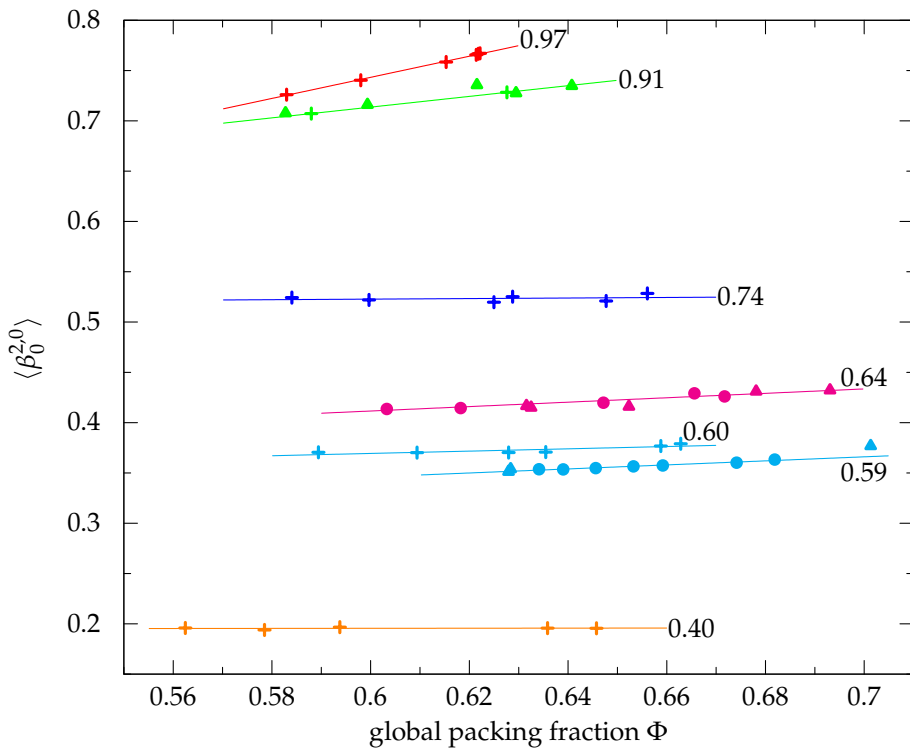
Figure 3.11: Average anisotropy index $\langle \beta_0^{2,0} \rangle$ of the Set Voronoi cells of the ellipsoid configurations as a function of the global packing fraction. The curve labels represent the aspect ratio α of the particles; (cross) 3D-Printer particles, (dot) placebo pills. These data are generated by the vertical tapping method described in section 2.2. In addition, triangles represent packings prepared with a range of different methods and container sizes.
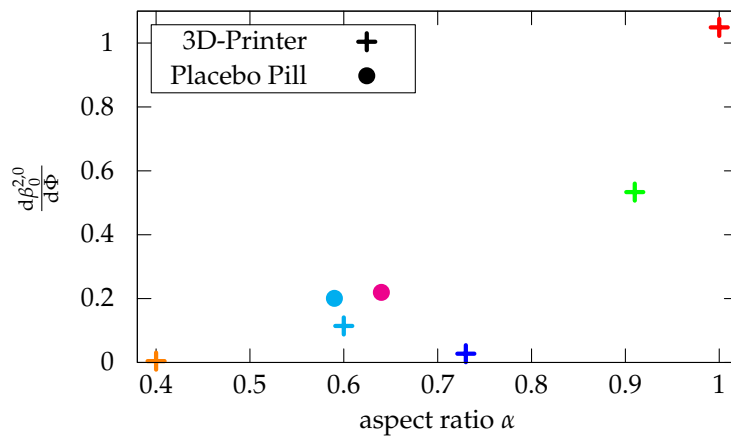

Figure 3.12: Slope of the linear fits to $\langle \beta_0^{2,0} \rangle (\Phi)$ as a function of the aspect ratio α, see figure 3.11.

3.6 Comparison to Numerical Data

3.6.1 Attainable Packing Fractions and Estimates from Discrete Element Method Simulations

The global packing fraction of the experimental data can be compared to numerical results. For frictionless and frictional ellipsoids settling into a container filled with a viscous liquid Delaney *et. al* [15] performed Discrete Element Method Simulations (DEM). Simulations with extremely high friction coefficient and very high viscosity lead to the loosest packings. This limit was named *sedimented loose packing limit* Φ_{SLP} [15]. These values should be a lower bound for the packing fraction for each aspect ratio. The upper bound is given by simulations of frictionless ellipsoids. In this case the packing fraction is independent on the viscosity. The upper bound estimated by Delaney *et. al* [15] coincides with the Lubachevsky Stillinger simulations performed by Donev *et. al* [16] despite their simulations have been without gravity.

The global packing fractions of the experimental datasets prepared by vertical tapping are now compared to these limits, see figure 3.13. In addition packings prepared with a range of different methods and container sizes are shown. The achieved packing fractions of all preparation methods lie in between these two limits.

It is difficult for experiments to probe the range of packing fractions for which disorder and jammed configurations can exist. Mostly due to friction, it is unclear if experiments can explore the whole range between the simulated lower and upper limits. Low packing fractions can only be achieved by a slowly settling of highly frictional particles. This can be accomplished by using a viscous liquid with a slightly smaller density than the one of the particles. To find the best way of preparing dense packings different preparation methods need to be tried. Tapping with more than 1500 taps can lead to denser packs. An experimental verification of both limits as well as the possibility of creating denser of looser packings need further investigations.

3.6.2 Voronoi Cell Anisotropy of Equilibrium Ellipsoid Ensembles and Jammed Ellipsoid Packings

A good reference system for ellipsoidal particles are non-static equilibrium fluids i.e. systems of ellipsoids with hard-core particle-particle interaction and no gravity in the system which is a well studied liquid crystal model. The orientations of the particles in the system are distributed randomly. Simulations of these systems are created with two methods. A Monte Carlo (MC) algorithm [60] was applied for low densities. The code for this simulation was provided by the group of Tanja Schilling[1]. For denser ensembles a Molecular Dynamics (MD) Simulation [13] has been used. Configurations of the MD ensembles were provided from Cristiano De Michele and Francesco Sciortino[2].

The anisotropy index $\langle \beta_0^{20} \rangle$ of non-static equilibrium fluids for different global packing fractions is shown in figure 3.14. It can be observed that the data of the

---

[1]Theory of Soft Condensed Matter, University of Luxembourg
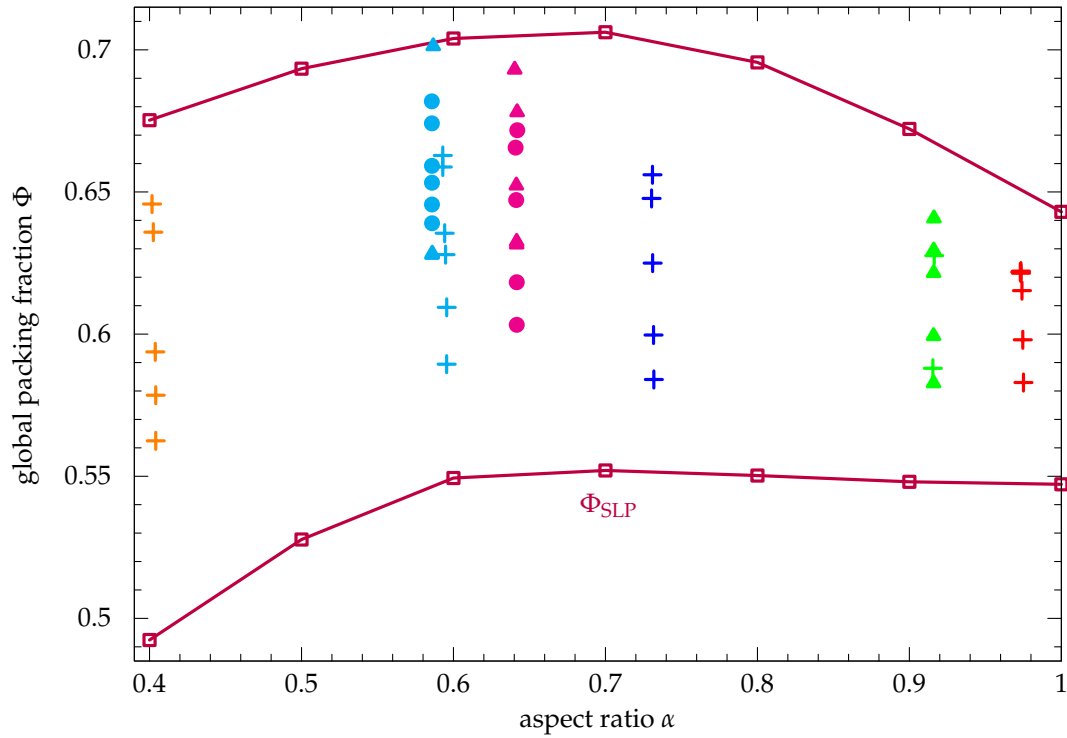[2]Department of Physics, University of Rome

Figure 3.13: The packing fractions of the experimental data compared to the upper and lower limits known from Discrete Element Method Simulations [15]. (cross) 3D-Printer particles, (dot) placebo pills, (triangle) packings prepared with different methods and container sizes, (square) upper and lower limits calculated by DEM Simulation. The upper limit is given by simulations of frictionless ellipsoids, the lower bound by simulation of the sedimentation of highly frictional particles in a viscous liquid. The lower bound was named *sedimented loose packing limit* Φ_{SLP}. (DEM data for upper and lower limits courtesy of Gary Delaney, CSIRO, Melbourne).

MC and MD simulations merge perfectly. In the limit $\Phi \to 0$ the anisotropy index is independent on the aspect ratio. This is obvious because in this limit the shape of the particles is irrelevant. In this limit the anisotropy index fits with the already known results for a Poisson Point Process [38]. For sphere-like particles the anisotropy index increases with the packing fraction implying that the cells get more isotropic. Ellipsoidal particles behave different the more ellipsoidal the shape of the particles becomes. Very ellipsoidal particles show a decrease of the anisotropy index with the packing fraction. A explanation for this behavior is that the shape of the Voronoi cell assimilates more the shape of its containing particle the denser the packing gets.

The anisotropy index for the jammed ellipsoid packs is smaller than the one for the densest fluid packing. This holds for sphere-like as well as for very ellipsoidal particles.

An interesting fact is that the anisotropy index in the MD simulations stays approximately constant for the aspect ratio $\alpha \approx 0.65$. Curiously, this coincides with the aspect ratio that produces the densest random packings in Lubachevsky Stillinger [16] and DEM simulations [14, 15].
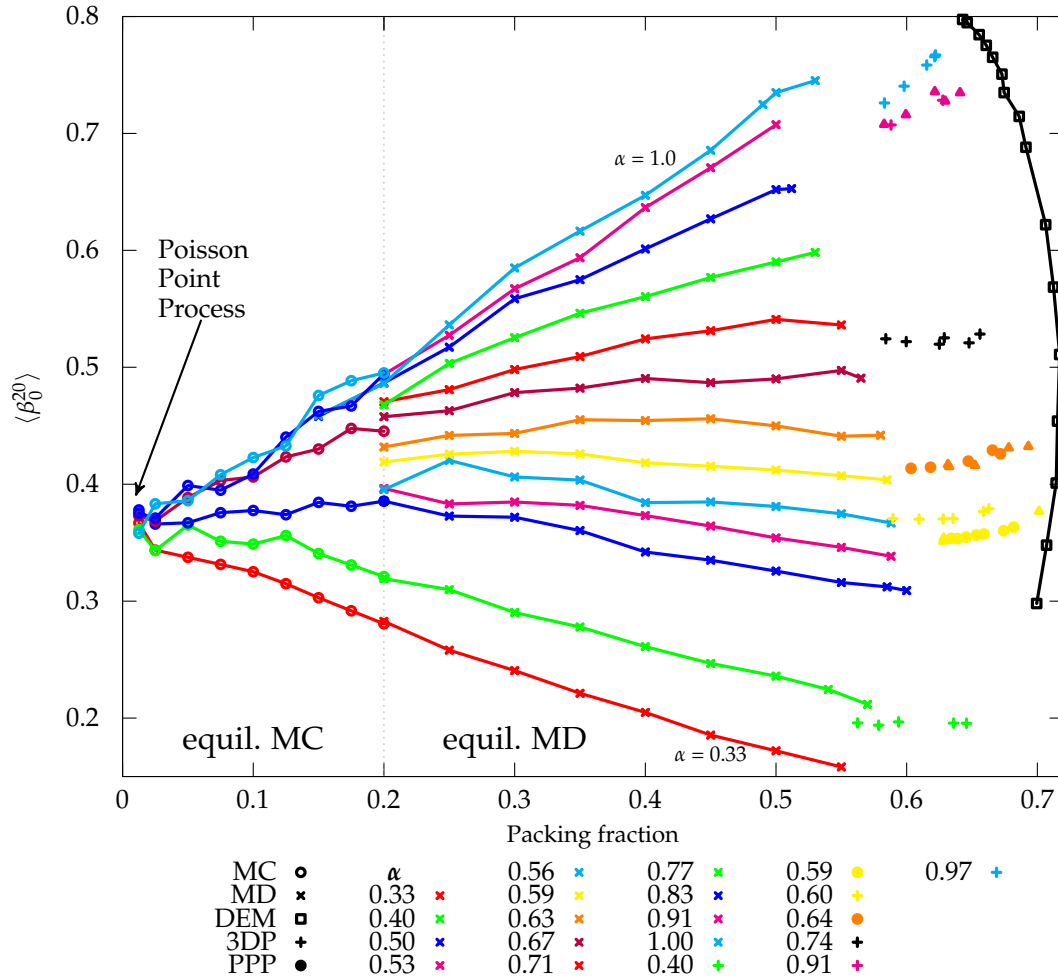
Figure 3.14: Average anisotropy index $\langle \beta_0^{20} \rangle$ of the Set Voronoi cells of the ellipsoids as function of the global packing fraction for equilibrium ellipsoid ensembles and static jammed ellipsoid packings. (MC) Monte Carlo Simulation; (MD) Molecular Dynamics Simulation; (DEM) Discrete Element Simulation; (3DP) Experimental data of 3D-Printer particles; (PPP) Experimental data of placebo pills. (MC data courtesy of Tanja Schilling, Universite du Luxembourg; MC data courtesy of Cristiano De Michele and Francesco Sciortino, University of Rome; DEM data courtesy of Gary Delaney, CSIRO, Melbourne).

4 Summary and Outlook

In this thesis the properties of jammed experimental packings of ellipsoidal particles have been studied. This study was based on the following analyzes:

- Experimental preparation of disordered packings of approximately 5000 ellipsoidal particles, each by a tapping protocol (ellipsoidal particles of three different types of materials, comprising in total 9 different aspect ratios).

- Recording of tomographic images of approximately 50 packings including digital reconstruction by segmentation and particle detection.

- Extraction of average (global) and local contact numbers from the tomographic datasets by a method based on "contact number scaling functions" of dilation width.

- Discussion of the alignment between the direction of gravity and the orientation of ellipsoids in experimental packings, to assess degree of order and homogeneity.

- Implementation of software to compute generalized (Set) Voronoi diagrams for ellipsoidal particles, by an algorithm based on the Voronoi Diagram of triangulated surfaces.

- Anisotropy analysis of the experimental and simulated ellipsoid configurations, using Minkowski tensor anisotropy measures applied to Voronoi cells.

- Comparison of experimental packing fractions and Voronoi cell anisotropy to Discrete Element Method simulations of jammed ellipsoids and to Monte Carlo and Molecular Dynamics data of equilibrium ellipsoid ensembles.

The analysis of the experimental packings and the comparison to numerical simulation have lead to the following results and conclusions:

- The distribution of the local packing fractions depends (in good approximation) only on the global packing fraction and seems to be independent on the aspect ratio. Deviations observed for only one particle type can be explained with spatial inhomogeneities of the local packing fraction.

- Packings of frictional ellipsoids are hyperstatic (mechanically overconstrained) in contrast to frictionless ellipsoids.

- The contact numbers of jammed ellipsoid packings predominantly depend on the global packing fraction. A weaker dependence on the aspect ratio α and the friction coefficient μ is observed.

- The packing fractions of the experimental datasets lie in between the two limits known from DEM simulations for the densest and looses possible values (under sedimentation) [15].

- The Minkowski anisotropy measure $\langle \beta_0^{20} \rangle$ of the Set Voronoi cells reveals an interesting difference in the local environment between jammed spheres and ellipsoid packings: While the Voronoi cell shape of spheres becomes more isotropic with increasing packing fraction (i.e. change shape [77]), the change of shape of the Voronoi cells of strongly oblate ellipsoid packings with the packing fraction is much weaker.

- Equilibrium fluids of ellipsoidal particles with different aspect ratios show different behavior in the average anisotropy index $\langle \beta_0^{20} \rangle$. Sphere-like particles show an increase in the anisotropy index with the packing fraction. The Voronoi cell shapes of ellipsoidal particles with a low aspect ratio α become more anisotropic with increasing packing fraction, while the cell shape of particles with large α does the opposite. This can be explained by the observation that the denser the packing the more the Voronoi cell adapts its shape to that of the particle.

Outlook

The results of this thesis suggest ideas for further investigation. In the following some interesting and open questions are briefly discussed.

- Does the average contact number of a jammed ellipsoid ensemble depend on the preparation history? For spheres a dependence was found numerically [1] but experimental results are missing. Lately it was found, that for ensembles of frictional tetrahedra the average contact number depends on the preparation history [55]. The particle detection in tomographic images and the contact number determination from the CNS function discussed in this thesis is of sufficiently good accuracy to address this problem, with experimental packings prepared by different protocols.

- For packing of spherical particles, a protocol-independent value for the densest achievable packing fraction of amorphous packings exists (*random close packing*). An interesting question is the nature, existence, type and protocol (in)dependence of the equivalent transition in ellipsoid packings. While a first order transition in spheres now appears as the most likely scenario, it is more complex in ellipsoids because of the degeneracy and a lack of knowledge of the crystal states. While particle friction and/or gravity prevented us from reaching even the maximally possible packing fractions for disordered configurations (in most cases), other experimental setups (such as shear cells, use of density-matched fluidized beds, ...) could give protocols to compact further and possibly induce crystal order. The geometric analysis described here will be useful to detect geometric signatures of this transition/behavior.
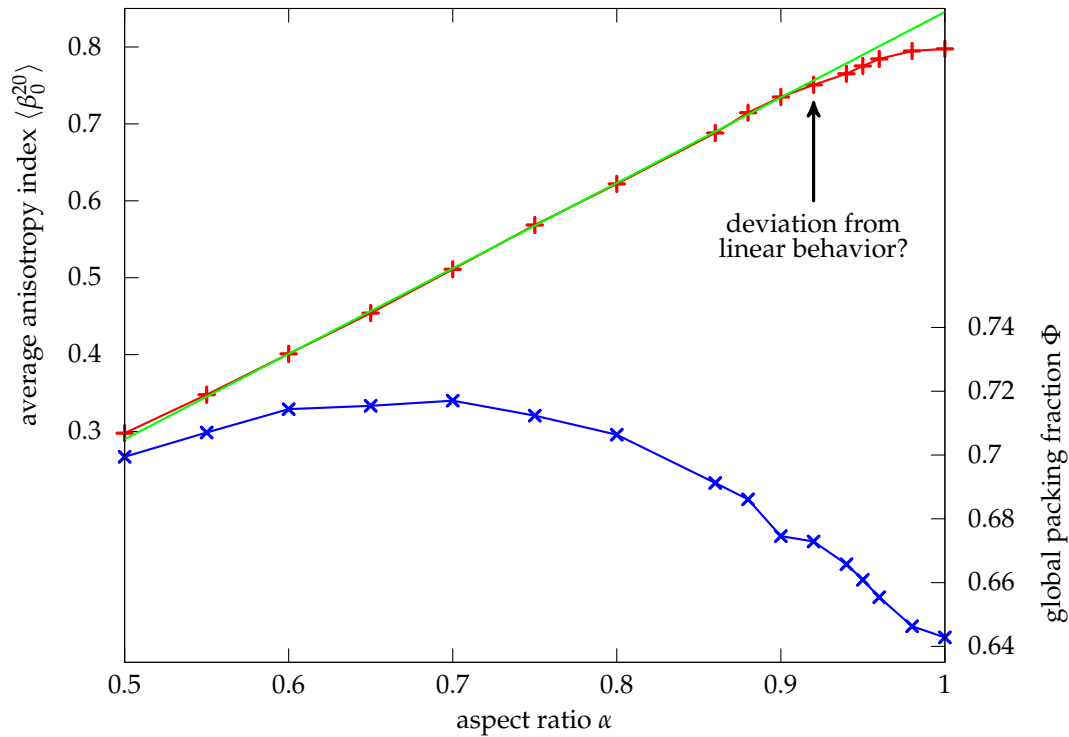
Figure 4.1: Average anisotropy index $\langle \beta_0^{20} \rangle$ (red, left y-axis) for maximally dense random packings of oblate ellipsoids created by DEM simulations [14]. Also the corresponding packing fraction (blue, right y-axis) is shown. The green line indicates the linear trend for small aspect ratios. (DEM configurations Courtesy of Gary Delaney (CSIRO, Melbourne).)

- How to measure the degree of order or crystallinity of an ellipsoid packing? With generalized Voronoi cells and Minkowski Tensor measures an in-depth understanding of local environment can be gained. In particular, order metrics could be defined either by quantifying deviations from a known crystalline reference state (analogous to the use of Q_6 in spheres) or by the study of typical features of local property distributions, such as Voronoi cell volumes, contact numbers, anisotropy, ...

- The anisotropy analysis of the densest random ellipsoid packings which can be obtained by DEM simulations of frictionless particles shows interesting features. First results can already be seen in figure 4.1. The average anisotropy index $\langle \beta_0^{20} \rangle$ of the Set Voronoi cells of the ellipsoidal particles shows a linear trend for small aspect ratios (green line). This changes at an aspect ratio of approximately $\alpha \approx 0.9$. At this point the anisotropy index shows a different behavior and heads towards the already known lower value for spheres [77]. The aspect ratio where this change in behavior seems to occur does not correspond to the aspect ratio with the maximal achievable packing fraction. The work of this

thesis (particularly the construction of the generalized Voronoi cell) can further elucidate there relationships between Voronoi cell shape and particle shape.

- Analyzing the transition from fluid to solid. For this purpose data of algorithms that can bridge a large range of packing fractions can be analyzed, e.g. the Lubachevsky Stillinger algorithm. This algorithm starts with a fluid state followed by an intermediate state which converges to a jammed state. It is not known if for ellipsoids with this algorithm crystalline or partially ordered states can be created. A study of geometric similarities and differences between ellipsoid configurations at very different densities (incl. equilibrium fluid, possible nematic order, amorphous or crystalline solids) will provide important reference data.

Acknowledgments

Bibliography

[1] AGNOLIN, I., AND ROUX, J.-N. Internal states of model isotropic granular packings. I. Assembling process, geometry, and contact networks. *Phys. Rev. E 76* (Dec 2007), 061302.

[2] ALESKER, S. Description of continuous isometry covariant valuations on convex sets. *Geom. Dedicata 74* (1999), 241–248.

[3] AMENTA, N., CHOI, S., AND KOLLURI, R. K. The power crust. In *Proceedings of the sixth ACM symposium on Solid modeling and applications* (New York, NY, USA, 2001), SMA '01, ACM, pp. 249–266.

[4] ARNS, C. H., KNACKSTEDT, M. A., PINCZEWSKI, W. V., AND MECKE, K. R. Euler-poincaré characteristics of classes of disordered media. *Phys. Rev. E 63*, 3 (2001), 031112.

[5] ASTE, T., SAADATFAR, M., AND SENDEN, T. J. Geometrical structure of disordered sphere packings. *Phys. Rev. E 71* (Jun 2005), 061302.

[6] ASTE, T., SAADATFAR, M., AND SENDEN, T. J. Local and global relations between the number of contacts and density in monodisperse sphere packs. *Journal of Statistical Mechanics: Theory and Experiment 2006*, 07 (2006), P07010.

[7] ASTE, T., AND WEAIRE, D. *The Pursuit of Perfect Packing*. Taylor & Francis Group, 2008.

[8] BARBER, C. B., DOBKIN, D. P., AND HUHDANPAA, H. The quickhull algorithm for convex hulls. *ACM Trans. Math. Softw. 22*, 4 (Dec. 1996), 469–483.

[9] BERNAL, J. D., AND MASON, J. Packing of spheres: Co-ordination of randomly packed spheres. *Nature 188* (1960).

[10] BLUM, H. Biological shape and visual science (part i). *Journal of Theoretical Biology 38*, 2 (1973), 205 – 287.

[11] BREIDENBACH, B. *Scalar and tensor-valued Minkowski functionals of spatially complex structures*. PhD thesis, Friedrich-Alexander Universität Erlangen-Nürnberg, 2007.

[12] CHIANG, M., WANG, X., LANDIS, F., DUNKERS, J., AND SNYDER, C. Quantifying the directional parameter of structural anisotropy in porous media. *Tissue Eng. 12*, 6 (2006), 1597–1606.

[13] DE MICHELE, C., SCHILLING, R., AND SCIORTINO, F. Dynamics of uniaxial hard ellipsoids. *Phys. Rev. Lett. 98* (Jun 2007), 265702.

[14] DELANEY, G. W., AND CLEARY, P. W. The packing properties of superellipsoids. *EPL (Europhysics Letters) 89*, 3 (2010), 34002.

[15] DELANEY, G. W., HILTON, J. E., AND CLEARY, P. W. Defining random loose packing for nonspherical grains. *Phys. Rev. E 83* (May 2011), 051305.

[16] DONEV, A., CISSE, I., SACHS, D., VARIANO, E. A., STILLINGER, F. H., CONNELLY, R., TORQUATO, S., AND CHAIKIN, P. M. Improving the density of jammed disordered packings using ellipsoids. *Science 303*, 5660 (2004), 990–993.

[17] DONEV, A., CONNELLY, R., STILLINGER, F. H., AND TORQUATO, S. Underconstrained jammed packings of nonspherical hard particles: Ellipses and ellipsoids. *Phys. Rev. E 75* (May 2007), 051304.

[18] DONEV, A., STILLINGER, F. H., CHAIKIN, P. M., AND TORQUATO, S. Unusually dense crystal packings of ellipsoids. *Phys. Rev. Lett. 92* (Jun 2004), 255506.

[19] EDWARDS, S., AND OAKESHOTT, R. Theory of powders. *Physica A: Statistical Mechanics and its Applications 157*, 3 (1989), 1080 – 1090.

[20] FELZENSZWALB, P., AND HUTTENLOCHER, D. Distance transforms of sampled functions. Tech. rep., 2004.

[21] FRENKEL, D., AND MULDER, B. The hard ellipsoid-of-revolution fluid. *Molecular Physics 55*, 5 (1985), 1171–1192.

[22] FRENKEL, D., MULDER, B. M., AND MCTAGUE, J. P. Phase diagram of a system of hard ellipsoids. *Phys. Rev. Lett. 52* (Jan 1984), 287–290.

[23] GOLDSTEIN, H. *Classical Mechanics*, 2nd ed. Addison-Wesley, 1980.

[24] GUDERLEI, R., KLENK, S., MAYER, J., SCHMIDT, V., AND SPODAREV, E. Algorithms for the computation of the Minkowski functionals of deterministic and random polyconvex sets. *Image Vision Comput. 25*, 4 (2007), 464–474.

[25] HADWIGER, H. Vorlesungen über Integralgeometrie. *Abhdl. Math. Sem. Hamburg 17* (1951), 69.

[26] HAJI-AKBARI, A., ENGEL, M., KEYS, A. S., ZHENG, X., PETSCHEK, R. G., PALFFY-MUHORAY, P., AND GLOTZER, S. C. Disordered, quasicrystalline and crystalline phases of densely packed tetrahedra. *Nature 462* (2009).

[27] HALES, T. C. The Kepler conjecture. *ArXiv Mathematics e-prints* (1998).

[28] HARRIGAN, T., AND MANN, R. Characterization of microstructural anisotropy in orthotropic materials using a second rank tensor. *J. Mater. Sci. 19* (1984), 761–767.

[29] HUG, D., SCHNEIDER, R., AND SCHUSTER, R. Integral geometry of tensor valuations. *Adv. in Appl. Math. 41* (2008), 482–509.

[30] HUG, D., SCHNEIDER, R., AND SCHUSTER, R. The space of isometry covariant tensor valuations. *St. Petersburg Math. J. 19* (2008), 137–158.

[31] INGEMAR, AND RAGNEMALM. Fast erosion and dilation by contour processing and thresholding of distance maps. *Pattern Recognition Letters 13*, 3 (1992), 161 – 166.

[32] INGLIS, D., AND PIETRUSZCZAK, S. Characterization of anisotropy in porous media by means of linear intercept measurements. *Int. J. Solids Struct. 40*, 5 (2003), 1243–1264.

[33] JACKSON, J. *Classical Electrodynamics*. John Wiley & Sons, 1975.

[34] JAEGER, H. M., AND NAGEL, S. R. Physics of the granular state. *Science 255*, 5051 (1992), 1523–1531.

[35] JERKINS, M., SCHRÖTER, M., SWINNEY, H. L., SENDEN, T. J., SAADATFAR, M., AND ASTE, T. Onset of mechanical stability in random packings of frictional spheres. *Phys. Rev. Lett. 101* (Jul 2008), 018301.

[36] JIN, Y., AND MAKSE, H. A. A first-order phase transition defines the random close packing of hard spheres. *Physica A: Statistical Mechanics and its Applications 389*, 23 (2010), 5362 – 5379.

[37] KAPFER, S. C., MICKEL, W., MECKE, K., AND SCHRÖDER-TURK, G. E. Jammed spheres: Minkowski tensors reveal onset of local crystallinity. *Phys. Rev. E 85* (Mar 2012), 030301.

[38] KAPFER, S. C., MICKEL, W., SCHALLER, F. M., SPANNER, M., GOLL, C., NOGAWA, T., ITO, N., MECKE, K., AND SCHRÖDER-TURK, G. E. Local anisotropy of fluids using Minkowski tensors. *Journal of Statistical Mechanics 2010* (2010), P11010:1–20.

[39] KERSCHER, M., MECKE, K., AND SCHÜCKER, P. Non-Gaussian morphology on large scales: Minkowski functionals of the reflex cluster catalogue. *Astron. Astrophys. 377* (2001), 1.

[40] KETCHAM, R., AND RYAN, T. Quantification and visualization of anisotropy in trabecular bone. *J. Microsc. 213*, 2 (2004), 158–171.

[41] LIMAYE, A. Drishti - volume exploration and presentation tool. Poster presentation,Vis 2006, Baltimore.

[42] LUBACHEVSKY, B. D., AND STILLINGER, F. H. Geometric properties of random disk packings. *Journal of Statistical Physics 60* (1990), 561–583. 10.1007/BF01025983.

[43] LUBACHEVSKY, B. D., STILLINGER, F. H., AND PINSON, E. N. Disks vs. spheres: Contrasting properties of random packings. *Journal of Statistical Physics 64* (1991), 501–524. 10.1007/BF01048304.

[44] LUCHNIKOV, V. A., MEDVEDEV, N. N., OGER, L., AND TROADEC, J.-P. Voronoi-delaunay analysis of voids in systems of nonspherical particles. *Phys. Rev. E 59* (Jun 1999), 7205–7212.

[45] MAN, W., DONEV, A., STILLINGER, F. H., SULLIVAN, M. T., RUSSEL, W. B., HEEGER, D., INATI, S., TORQUATO, S., AND CHAIKIN, P. M. Experiments on random packings of ellipsoids. *Phys. Rev. Lett. 94*, 19 (May 2005), 198001.

[46] MANTZ, H., JACOBS, K., AND MECKE, K. Utilising Minkowski functionals for image analysis. *J. Stat. Mech.: Theory E. 12* (2008), 12015.

[47] M'ARTHUR, N. Principal radii of curvature at a point on an ellipsoid. *Edinburgh Mathematical Notes 24* (1929), xvi–xvii.

[48] MATHIEU, L., MUELLER, T., BOURBAN, P., PIOLETTI, D., MULLER, R., AND MANSON, J. Architecture and properties of anisotropic polymer composite scaffolds for bone tissue engineering. *Biomaterials 27*, 6 (2006), 905–916.

[49] MECKE, K. *Integralgeometrie in der statistischen Physik*. Harri Deutsch (Frankfurt), 1994.

[50] MECKE, K. Morphological characterization of patterns in reaction-diffusion systems. *Phys. Rev. E 53*, 5 (1996), 4794–4800.

[51] MECKE, K. Integral geometry and statistical physics. *Int. J. Mod. Phys. B 12* (1998), 861–899.

[52] MECKE, K. Additivity, convexity, and beyond: Applications of Minkowski functionals in statistical physics. In *Statistical Physics and Spatial Statistics – The Art of Analyzing and Modeling Spatial Structures and Patterns* (2000), K. Mecke and D. Stoyan, Eds., vol. 554 of *Lecture Notes in Physics*, Springer Verlag, pp. 111–184.

[53] MECKE, K., BUCHERT, T., AND WAGNER, H. Robust morphological measures for large-scale structure in the universe. *Astron. Astrophys. 288* (1994), 697.

[54] MECKE, K., AND WAGNER, H. Euler characteristic and related measures for random geometric sets. *J. Stat. Phys. 64* (1991), 843–.

[55] NEUDECKER, M., ULRICH, S., HERMINGHAUS, S., AND SCHRÖTER, M. Jamming of frictional tetrahedra. *ArXiv e-prints* (Feb. 2012).

[56] NYE, J. *Physical Properties of Crystals*. Oxford Science Publications, 1985.

[57] ODGAARD, A. Three-dimensional methods for quantification of cancellous bone architecture. *Bone 20*, 4 (1997), 315 – 328.

[58] O'Hern, C. S., Silbert, L. E., Liu, A. J., and Nagel, S. R. Jamming at zero temperature and zero applied stress: The epitome of disorder. *Phys. Rev. E 68* (Jul 2003), 011306.

[59] Okabe, A., Boots, B., Sugihara, K., and Chiu, S. N. *Spatial tessellations: Concepts and applications of Voronoi diagrams*, 2nd ed. Probability and Statistics. Wiley, NYC, 2000. 671 pages.

[60] Pfleiderer, P., Milinkovic, K., and Schilling, T. Glassy dynamics in monodisperse hard ellipsoids. *EPL (Europhysics Letters) 84*, 1 (2008), 16003.

[61] Pfleiderer, P., and Schilling, T. Simple monoclinic crystal phase in suspensions of hard ellipsoids. *Phys. Rev. E 75* (Feb 2007), 020402.

[62] Philippe, P., and Bideau, D. Compaction dynamics of a granular medium under vertical tapping. *EPL (Europhysics Letters) 60*, 5 (2002), 677.

[63] Press, W., Teukolsky, S., Vetterling, W., and Flannery, B. *Numerical Recipes, The Art of Scientific Computing*, 3 ed. Cambridge University Press, 2007.

[64] Radin, C. Random close packing of granular matter. *Journal of Statistical Physics 131* (2008), 567–573. 10.1007/s10955-008-9523-1.

[65] Radu, M., Pfleiderer, P., and Schilling, T. Solid-solid phase transition in hard ellipsoids. *The Journal of Chemical Physics 131*, 16 (2009), 164513.

[66] Ras, T., Schilling, R., and Weigel, M. Regular packings on periodic lattices. *Phys. Rev. Lett. 107* (Nov 2011), 215503.

[67] Richard, P., Nicodemi, M., Delannay, R., Ribière, P., and Bideau, D. Slow relaxation and compaction of granular systems. *Nature Materials 4*, 2 (2005), 121–128.

[68] Saadatfar, M., Shepard, A. N. P., and Knackstedt, M. K. A. *Grain Partitioning and its Applications*. ISTE, 2010, pp. 269–276.

[69] Schneider, P. J., and Eberly, D. *Geometric Tools for Computer Graphics*. Elsevier Science Inc., New York, NY, USA, 2002.

[70] Schneider, R. Curvature measures of convex bodies. *Ann. Math. Pura Appl. 11* (1978), 101–134.

[71] Schneider, R. *Convex Bodies: The Brunn-Minkowski Theory*. Cambridge University Press, 1993.

[72] Schneider, R., and Weil, W. *Stochastic and Integral Geometry (Probability and Its Applications)*. Springer, 2008.

[73] Schröder-Turk, G. E., Kapfer, S. C., Breidenbach, B., Beisbart, C., and Mecke, K. Tensorial Minkowski functionals and anisotropy measures for planar patterns. *J. Microsc. 238* (2010), 57–74.

[74] SCHRÖDER-TURK, G. E., MICKEL, W., KAPFER, S., SCHALLER, F., HUG, D., BREIDENBACH, B., AND MECKE, K. Minkowski Tensors of anisotropic spatial structure. *arXiv e-prints* (2010).

[75] SCHRÖDER, G., RAMSDEN, S., CHRISTY, A., AND HYDE, S. Medial surfaces of hyperbolic structures. *The European Physical Journal B - Condensed Matter and Complex Systems 35* (2003), 551–564. 10.1140/epjb/e2003-00308-y.

[76] SCHRÖDER-TURK, G. E., MICKEL, W., KAPFER, S. C., KLATT, M. A., SCHALLER, F. M., HOFFMANN, M. J. F., KLEPPMANN, N., ARMSTRONG, P., INAYAT, A., HUG, D., REICHELSDORFER, M., PEUKERT, W., SCHWIEGER, W., AND MECKE, K. Minkowski tensor shape analysis of cellular, granular and porous structures. *Advanced Materials 23*, 22-23 (2011), 2535–2553.

[77] SCHRÖDER-TURK, G. E., MICKEL, W., SCHRÖTER, M., DELANEY, G. W., SAADATFAR, M., SENDEN, T. J., MECKE, K., AND ASTE, T. Disordered spherical bead packs are anisotropic. *EPL (Europhysics Letters) 90*, 3 (2010), 34001.

[78] SCOTT, G. D., AND KILGOUR, D. M. The density of random close packing of spheres. *Journal of Physics D: Applied Physics 2*, 6 (1969), 863.

[79] SIDDIQI, K., AND PIZER, S. *Medial Representations: Mathematics, Algorithms and Applications.* Computational Imaging and Vision. Springer, 2008.

[80] SILBERT, L. E., ERTAŞ, D., GREST, G. S., HALSEY, T. C., AND LEVINE, D. Geometry of frictionless and frictional sphere packings. *Phys. Rev. E 65* (Feb 2002), 031304.

[81] SOILLE, P. *Morphological Image Analysis: Principles and Applications*, 2 ed. Springer-Verlag New York, Inc., Secaucus, NJ, USA, 2003.

[82] SONG, C., WANG, P., AND MAKSE, H. A. A phase diagram for jammed matter. *Nature 453* (2008), 629–632.

[83] STARR, F., SASTRY, S., DOUGLAS, J., AND GLOTZER, S. What do we learn from the local geometry of glass-forming liquids? *Phys. Rev. Lett. 89*, 12 (Aug 2002), 125501.

[84] STEINHARDT, P. J., NELSON, D. R., AND RONCHETTI, M. Bond-orientational order in liquids and glasses. *Phys. Rev. B 28* (Jul 1983), 784–805.

[85] TORQUATO, S., AND STILLINGER, F. H. Jammed hard-particle packings: From kepler to bernal and beyond. *Rev. Mod. Phys. 82* (Sep 2010), 2633–2672.

[86] VAN HECKE, M. Jamming of soft particles: geometry, mechanics, scaling and isostaticity. *Journal of Physics: Condensed Matter 22*, 3 (2010), 033101.

[87] WALD, M., VASILIC, B., SAHA, P., AND WEHRLI, F. Spatial autocorrelation and mean intercept length analysis of trabecular bone anisotropy applied to in vivo magnetic resonance imaging. *Med. Phys. 34*, 3 (2007), 1110–1120.

[88] WHITEHOUSE, W. The quantitative morphology of anisotropic trabecular bone. *J. Microsc. 101*, 2 (1974), 153–168.

[89] WILLIAMS, T., AND KELLEY, C. Gnuplot - an interactive plotting program.

Erklärung

Hiermit erkläre ich, dass ich die vorliegende Diplomarbeit selbständig angefertigt habe und keine anderen als die in der Arbeit ausdrücklich genannten Hilfsmittel verwendet habe.

Erlangen, 4. Mai 2012   Fabian Schaller